

# Discovering explicit Reynolds-averaged turbulence closures for turbulent separated flows through deep learning-based symbolic regression with non-linear corrections

Hongwei Tang,<sup>1</sup> Yan Wang,<sup>1, 2, a)</sup> Tongguang Wang,<sup>1</sup> and Linlin Tian<sup>1</sup>

<sup>1)</sup>*Jiangsu Key Laboratory of Hi-Tech Research for Wind Turbine Design, Nanjing University of Aeronautics and Astronautics, 29 Yudao St., Nanjing 210016, China*

<sup>2)</sup>*State Key Laboratory of Mechanics and Control of Mechanical Structures, Nanjing University of Aeronautics and Astronautics, 29 Yudao St., Nanjing 210016, China*

This work introduces a novel data-driven framework to formulate explicit algebraic Reynolds-averaged Navier-Stokes (RANS) turbulence closures. Recent years have witnessed a blossom in applying machine learning (ML) methods to revolutionize the paradigm of turbulence modeling. However, due to the black-box essence of most ML methods, it is currently hard to extract interpretable information and knowledge from data-driven models. To address this critical limitation, this work leverages deep learning with symbolic regression methods to discover hidden governing equations of Reynolds stress models. Specifically, the Reynolds stress tensor is decomposed into linear and non-linear parts. While the linear part is taken as the regular linear eddy viscosity model, a long short-term memory neural network is employed to generate symbolic terms on which tractable mathematical expressions for the non-linear counterpart are built. A novel reinforcement learning algorithm is employed to train the neural network to produce best-fitted symbolic expressions. Within the proposed framework, the Reynolds stress closure is explicitly expressed in algebraic forms, thus allowing for direct functional inference. On the other hand, the Galilean and rotational invariance are craftily respected by constructing the training feature space with independent invariants and tensor basis functions. The performance of the present methodology is validated through numerical simulations of three different canonical flows that deviate in geometrical configurations. The results demonstrate promising accuracy improvements over traditional RANS models, showing the generalization ability of the proposed method. Moreover, with the given explicit model equations, it can be easier to interpret the influence of input features on generated models.

## I. INTRODUCTION

Accurate predictions of turbulent flows are of paramount importance for many engineering applications of computational fluid dynamics (CFD). With the increasing availability of computational resources over the last two decades, scale-resolving simulations such as large eddy simulation (LES) and direct numerical simulation (DNS) have gained widespread applications. While these methods indeed provide plenty of detailed insights into fluid flow physics, an immediate difficulty relates to the computational cost, which could be prohibitively large for many practical applications in physics and engineering sciences. By contrast, the computationally lower cost and superior robustness leave the Reynolds-averaged Navier-Stokes (RANS) models still the most widely used tool in industrial simulations. This scenario will remain unchanged into the coming decades<sup>1</sup>. However, the predictive accuracy of RANS equations could be severely plagued with the unsolved closure problem deeply rooted in RANS governing equations. Such deficiency is strikingly serious for flow with complex geometries and large separations<sup>2</sup>. Since the pioneering work of Boussinesq to develop a mathematical description of Reynolds stress by introducing the concept of eddy viscosity, there has been a continuous attempt to formulate more accurate RANS turbulence models.

In recent years, thanks to the rapid advancement of high-performance computing architectures and the increasingly ac-

cessible high-fidelity flow data, the emerging machine learning (ML) and data science techniques provide a new alternative in the analysis and understanding of turbulent flows<sup>3,4</sup>. This paradigm has been blossoming in turbulence modeling research. For example, Cheung *et al.*<sup>5</sup> applied Bayesian techniques to calibrate the parameters of a traditional turbulence model against experimental data. Yan, Zhang, and Chen<sup>6</sup> took the ML method to augment a turbulence model to enhance its prediction in separation flow. These works try to improve the turbulence model performance without breaking the Boussinesq assumption.

Rather than correcting the governing equations of existing turbulence models, another research subject is constructing new constitutive models for Reynolds stress tensors. The related ideas are generally conceptualized from the insightful hypothesis made by Pope<sup>7</sup>, where the anisotropic Reynolds stress is expressed as an algebraic tensor polynomial. For example, Wu, Xiao, and Paterson<sup>8</sup> built a framework for enhancing RANS turbulence models with carefully designed input features to ensure Galilean and rotational invariance of the model predictions. Following this work, Yin *et al.*<sup>9</sup> then improved the approach by reconsidering the criterion for selecting input features. Another school of thought is to recast the neural network architectures. The pioneering effort could trace back to the work by Ling, Kurzawski, and Templeton<sup>10</sup>, in which they proposed a novel deep neural network architecture that integrated a set of tensor basis into neural networks to model anisotropic Reynolds stress tensor. Following this effort, Jiang *et al.*<sup>11</sup> recently presented a ML-based turbulence modeling framework in which two parallel ML modules are combined to directly infer structural and parametric representations of

<sup>a)</sup>Electronic mail: aerowangy@nuaa.edu.cn

turbulence physics, respectively.

Despite the improved performance presented in the above-mentioned works and many others<sup>12,13</sup>, the black-box nature of most ML methods hampers the understanding of obtained data-driven models, making it difficult to provide physical interpretations and infer new flow physics. On the other hand, it may also increase the difficulty for disseminating the learned models to end users since there are no explicit mathematical equations.

Recently, symbolic regression approaches have gained a renaissance in ML community. The task of symbolic regression is to find a symbolic function that best predicts the target given input variables. Some researchers have applied these approaches to detect hidden fluid properties, and the relevant results present towering promise and preliminary success<sup>14,15</sup>. Driven by such prevalence, various symbolic regression methods, such as gene expression programming (GEP) and sparse regression, have been introduced to derive new Reynolds stress models that can be expressed in explicit algebraic forms. Weatheritt and Sandberg<sup>16</sup> proposed an expansion of the GEP method to model Reynolds stress tensor from high-fidelity data. This work was then further developed by Zhao *et al.*<sup>17</sup> by integrating the CFD simulations with GEP training process. The learning target was set as the velocities rather than the Reynolds stress itself. However, due to the GEP being by nature a non-deterministic method, the mathematical form of the model it discovers can vary from different runs. By contrast, Schmelzer, Dwight, and Cinnella<sup>18</sup> introduced a deterministic symbolic regression method to infer algebraic stress models by leveraging the fast function extraction method. This method can identify the relevant candidate functions by imposing a sparsity constraint. Similarly, the sparse identification of non-linear dynamics approach was employed by Beetham and Capecehatro<sup>19</sup> to formulate new turbulence closures with affordable interpretability and transportability.

The success of symbolic regression methods in discovering turbulence models motivates the present work, in which a new model discovery strategy based on the deep symbolic regression (DSR) method<sup>20</sup> is introduced to formulate Reynolds stress models that can be explicitly expressed in algebraic forms. The DSR method is a deterministic methodology and is built on the combination of deep learning and symbolic regression techniques. During the model training process, the DSR approach can ensure that all samples adhere to all constraints, without rejecting samples post hoc. In contrast, the GEP method may produce operations that violate imposed constraints, thus requiring rejections post hoc. This process could be problematic. In addition, most symbolic regression methods suffer from the expectation problem. That is, these methods are fundamentally designed to optimize the expected performance. However, symbolic regression generally aims to maximize the performance of few (or single) best-fitting samples. This problem can be solved by leveraging the risk-seeking reinforcement learning (RL) algorithm, as is done in the present work.

In a sense, the utilization of RL could be one of the most appealing features of DSR method. It is a natural choice since symbolic space can be considered as an environment where

states and actions are given as symbolic tokens<sup>21</sup>. Unlike supervised learning which needs a knowledgeable external supervisor to provide labeled data, RL is designed for decision-making problems. It generally does not need data to be labeled and can learn through trial and error<sup>22</sup>. RL has gained unprecedented interest in many domains, such as robotics<sup>23</sup>, mathematics<sup>24</sup>, and games<sup>25</sup>. Recent years also have witnessed a blossoming of RL in fluid mechanics<sup>26</sup>. Some typical applications include the behavior adaptation of swimmers<sup>27,28</sup>, active flow control for drag reduction<sup>29–32</sup> and conjugate heat transfer<sup>33,34</sup>, and aerodynamic shape optimization<sup>35,36</sup>.

The application of RL in formulating turbulence models is at a very early stage, with most works focusing on the development of reliable subgrid-scale models for LES. The pioneering study is proposed by Novati, de Laroussilhe, and Koumoutsakos<sup>37</sup>, in which RL is leveraged to adjust the coefficients of the eddy-viscosity closure model, in order to reproduce the energy spectrum of homogeneous isotropic turbulence (HIT) predicted by DNS. This approach was then further developed by Kim *et al.*<sup>38</sup> for wall-bounded turbulence. The main advantage of RL against supervised learning is that RL could address the distinction between a priori and a posteriori evaluation and account for compounding modeling errors<sup>37</sup>. In a similar but conceptually different study, Bae and Koumoutsakos<sup>39</sup> applied RL for the discovery of wall models for LES. Moreover, supervised learning could be ill-posed for turbulence modeling in implicit filtered LES due to labeled filter form is not available. This challenge can be alleviated by RL, as is done by Kurz, Offenhäuser, and Beck<sup>40</sup>, who applied RL with convolutional neural networks to find an optimal eddy-viscosity for implicitly filtered LES of HIT.

By integrating the invariants and tensor basis in the DSR model training method, the objective of this work is to develop a new method for discovering turbulence closures in explicit algebraic forms, with emphases on

1. Interpretability: the obtained model can be explicitly expressed as a finite tensor polynomial, making it easier to infer the underlying physics and reveal the constitutive relationship between input features and output targets.
2. Galilean and rotational invariance: by constructing the feature space and the neural network architecture with an integrity tensor basis and invariants, both Galilean and rotational invariance can be achieved.
3. Transportability: it is straightforward to implement the learned model in RANS solvers since it is expressed as mathematical expressions. Consequently, there is no need to redeploy the production systems.

The remainder of this paper is organized as follows. First, a brief introduction to the main governing equations used for performing simulation is provided in Section II, along with the general theory and implementation details underlying the construction of training methods. Next, three canonical flows with notably different geometry are selected as testing cases. And the simulation results that highlight the robustness and generalization ability of the proposed approach are detailed in

Section III. Finally, a summary of the contribution is demonstrated in Section IV.

## II. METHODOLOGY

### A. Governing equations

In this work, the incompressible turbulent flow is taken to illustrate the modeling framework. The governing RANS equations read

$$\nabla \cdot \mathbf{u} = 0, \quad (1)$$

$$\frac{\partial \mathbf{u}}{\partial t} + \mathbf{u} \cdot \nabla \mathbf{u} = -\nabla p + \nu \nabla^2 \mathbf{u} - \nabla \cdot \boldsymbol{\tau}, \quad (2)$$

where  $\mathbf{u}$ ,  $p$ , and  $\nu$  are the mean velocity, mean pressure (normalized by density), and viscosity, respectively.  $\boldsymbol{\tau}$  is the Reynolds stress accounting for unresolved turbulence. Herein the Reynolds stress is unknown and needs to be closed by a mathematical model. Hence, the effects regarding the discretization schemes and numerical algorithms aside, a turbulence closure model acts as the most critical factor in the prediction accuracy of RANS equations. In the present work, a symbolic regression method based on deep learning techniques will be leveraged to produce extra anisotropic terms for Reynolds stress, to improve the predictive accuracy of RANS equations.

### B. Baseline RANS turbulence model

The most commonly used theory for the closure of Reynolds stress tensor is the linear eddy viscosity model (LEVM) proposed by Boussinesq

$$\boldsymbol{\tau} = \frac{2}{3} k \mathbf{I} - \nu_t \left[ \nabla \mathbf{u} + (\nabla \mathbf{u})^T \right], \quad (3)$$

where  $\mathbf{I}$  denotes the identity matrix,  $(\cdot)^T$  means transposition.  $\nu_t$  indicates the turbulent viscosity which is unknown and needs to be estimated by one RANS turbulence model. This assumption is widely used at the expense of accuracy and is susceptible to influences from certain flow configurations, as will be discussed in the following sections.

The data-driven turbulence model framework developed in the present study is based on the widely applied standard  $k - \varepsilon$  model<sup>41</sup>, in which the equations for the turbulent kinetic energy  $k$  and the turbulent dissipation rate  $\varepsilon$  are written as

$$\frac{\partial k}{\partial t} + \mathbf{u} \cdot \nabla k = \nabla \cdot (\mathbf{v}_{eff,k} \nabla k) + P_k - \varepsilon, \quad (4)$$

$$\frac{\partial \varepsilon}{\partial t} + \mathbf{u} \cdot \nabla \varepsilon = \nabla \cdot (\mathbf{v}_{eff,\varepsilon} \nabla \varepsilon) + C_{\varepsilon 1} \frac{\varepsilon}{k} P_k - C_{\varepsilon 2} \frac{\varepsilon^2}{k}, \quad (5)$$

where other relations for closing the transport equations are

$$\mathbf{v}_{eff,k} = \mathbf{v} + \frac{\nu_t}{\sigma_k}, \quad \mathbf{v}_{eff,\varepsilon} = \mathbf{v} + \frac{\nu_t}{\sigma_\varepsilon}, \quad P_k = -\boldsymbol{\tau} : \nabla \mathbf{u}. \quad (6)$$

Starting with the Boussinesq eddy viscosity assumption, the turbulent eddy viscosity  $\nu_t$  is given as

$$\nu_t = \frac{C_\mu k^2}{\varepsilon}. \quad (7)$$

Furthermore, the five model coefficients  $C_\mu, C_{\varepsilon 1}, C_{\varepsilon 2}, \sigma_k, \sigma_\varepsilon$  are flow-specific tuning and fudge parameters. In the context of this work, the standard values due to Launder and Sharma<sup>41</sup> are adopted. The whole set of these coefficients is shown below

$$C_\mu = 0.09, C_{\varepsilon 1} = 1.44, C_{\varepsilon 2} = 1.92, \sigma_k = 1.0, \sigma_\varepsilon = 1.3. \quad (8)$$

It is worth stressing that these constant coefficients are calibrated by simplified theories and limited experiments. In addition, the standard  $\varepsilon$  equation (Eq. 5) is not based on the exact transport equation. It is best viewed as an empirical equation since only large-scale flow motions are considered in its derivation. As a consequence, the accuracy of standard  $k - \varepsilon$  model is possibly impeded in turbulent separated flow simulations, which can be well solved by the data-driven turbulence model developed in this work.

### C. Data-driven RANS turbulence framework

Although the Boussinesq assumption has been widely used in turbulence modeling research, it cannot produce an adequate approximation to Reynolds stress. In addition, it could become invalid in flow simulations featuring large separations<sup>1,2</sup>. The goal of this work is to introduce a data-driven turbulence model with explicit mathematical expressions to increase the accuracy of traditional RANS simulations. Rather than simply correcting the parameters of traditional turbulence models, this work seeks a more comprehensive effort to improve the Boussinesq assumption by adding an extra stress tensor  $\mathbf{b}^\perp$  as

$$\boldsymbol{\tau} = \frac{2}{3} k \mathbf{I} - \nu_t \left[ \nabla \mathbf{u} + (\nabla \mathbf{u})^T \right] + k \mathbf{b}^\perp. \quad (9)$$

The  $\mathbf{b}^\perp$  represents the non-linear part of Reynolds stress tensor (detailed in next section). Taking  $\mathbf{b}^\perp$  as the learning target, the framework used in this work is illustrated in Fig. 1. This framework consists of two key phases. During the training phase, a number of RANS and DNS/LES flow pairs are utilized to build a regression model. The training process aims to minimize the discrepancy (the training error in Fig. 1) between ML predictions and high-fidelity data. Then, the obtained ML model is used to predict the target flow fields for new unseen flows. This process corresponds to the prediction phase. The corrected fields are subsequently propagated through the modified RANS solver to improve the baseline RANS predictions. To avoid the divergence of the data-driven simulations, a common practice is to freeze the predictions of the ML model. More specifically, the ML model is only called at the initial time and its predictions are then kept as constants when solving the RANS equations. This mode is usually referred to as loose coupling and is used in present work. On the contrary, tight coupling requires that the ML model participates in the iterative process of RANS simulations. And readers who are

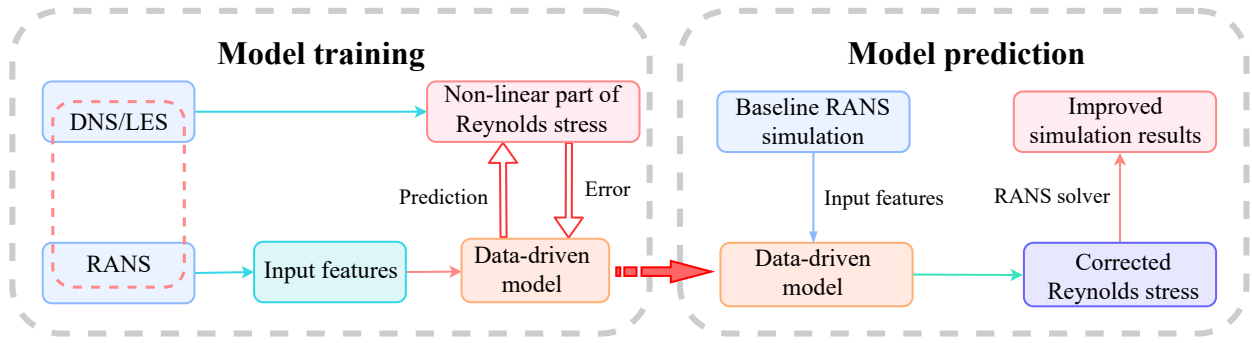


FIG. 1. A schematic of the framework for data-driven turbulence modeling. The overall process includes two stages: training (left block) and prediction (right block).

interested in this subject can refer to the review by Duraisamy<sup>4</sup>.

The framework shown in Fig. 1 has permeated the area of data-driven turbulence modeling research, with various learning targets used by different researchers. In the context of this work, the symbolic regression method based on deep learning is selected to serve as the ML model. The details about the construction of DSR method and turbulence modeling schemes will be outlined in the following sections.

### 1. Symbolic regression based on deep learning

The deep neural network could be the most commonly used regression model for building data-driven models. An immediate difficulty relates to its interpretability, which tends to be prohibitively tricky since deep learning models are highly recursive<sup>42</sup>. By contrast, taking compact symbolic formulations to describe physical systems can provide inherently interpretable insights, thus making it easier to infer with existing theories. In this study, based on the DSR approach initially proposed by Petersen *et al.*<sup>20</sup>, a data-driven framework is developed for understanding the mathematical relationships among variables in a turbulent flow system.

DSR is a gradient-based approach for symbolic regression. The core idea of DSR is to use a large model to search the space of a small model. More specifically, DSR employs expressive recurrent neural networks (RNNs) to generate best-fitting symbolic expressions under some pre-specified constraints. In DSR, each token for constructing symbolic expressions is sampled from the outputs of a special kind of RNNs, the long short-term memory (LSTM) neural network. The fitness of symbolic expressions is then used as the reward function to train the neural networks by a novel RL algorithm. By this means, it is possible to seamlessly combine the representational capacity of deep learning models and the natural interpretability of symbolic expressions. An overview of DSR approach is illustrated in Fig. 2, and the whole training process can be broadly summarized as follows

1. Design inputs to LSTM neural networks. LSTM neural networks can learn the dependence among data sequences, which means the obtained token would be par-

tially determined by previously sampled tokens. In this sense, the search space for symbolic expressions is inherently hierarchical. To ensure the hierarchical information is well-captured, DSR leverages the parent and sibling nodes of the token being sampled as inputs to the LSTM networks. Consequently, the sampled token is mainly determined by its adjacent nodes in the expression tree.

2. Impose a priori constraints to the search space. Under the DSR framework, several domain-agnostic constraints are applied to reduce the search space
  - The minimum and maximum length of symbolic expressions have to be specified before training starts.
  - A binary operator at least has one child that is non-constant.
  - The child of a unary operator should not be the inverse of that operator.
  - The descendants of trigonometric operators cannot contain trigonometric operators.

These constraints are concurrently applied in the training process by ditching the tokens that would violate any one of the constraints. Such a sampling process craftily respects all pre-specified limits without rejecting samples post hoc, which makes the DSR method more amenable to complex tasks.

3. Choose the reward function. Within the DSR approach, the neural networks are trained by a risk-seeking policy gradient algorithm, and the performance of sampled expressions is evaluated with a reward function. The symbolic expressions that best fit the training dataset could vary with different reward functions. This feature will be discussed in detail in the next section.
4. Optimize constants in expressions. The sampled expressions may include constants that need to be optimized to maximize the reward function. In DSR, an inner optimization loop for each sampled expression is performed before executing each training epoch.

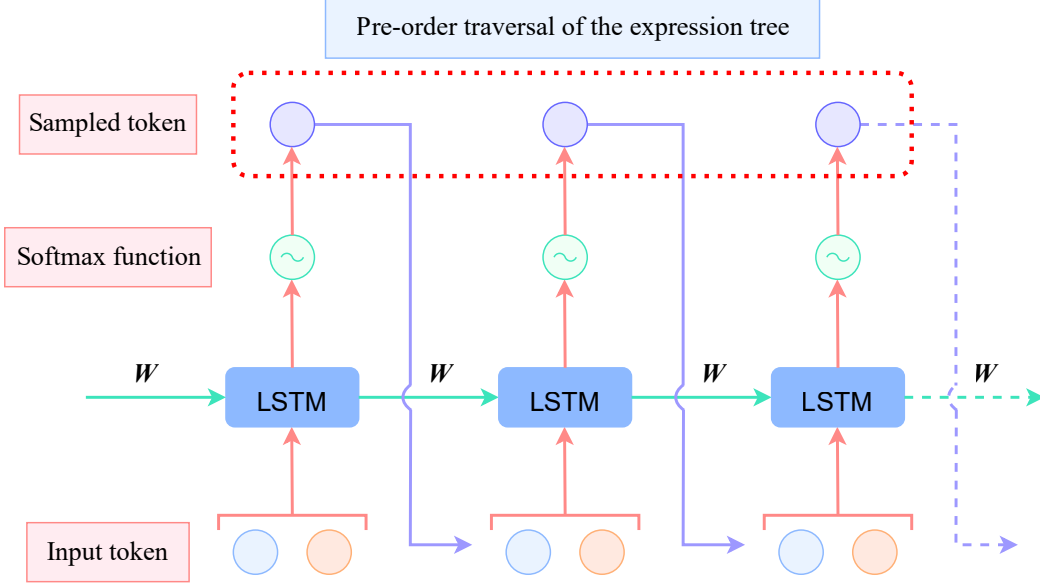


FIG. 2. An overview for generating expressions with DSR methodology.

As can be observed in Fig. 2, a softmax activation function is used in the output layer. Therefore, the LSTM neural networks would emit a probabilistic distribution over symbolic expressions. The token with the highest probability is then sampled to constitute the mathematical expressions. If the token being sampled is against the pre-defined constraints, however, its sampling probability would be reset to zero. After finishing the training process, the pre-order traversal of sampled tokens can represent the symbolic expression tree in which internal nodes are mathematical operators and terminal nodes are input variables or constants. The mathematical expression can then be generated by the pre-order traversal of its corresponding expression tree.

As aforementioned, within the DSR framework, a novel RL algorithm, known as the risk-seeking policy gradient algorithm, is chosen to train the neural network model. The objective of symbolic regression is to maximize the best-case performance. This objective could be plagued by traditional policy gradient methods since they are fundamentally designed to optimize the expected performance (the performance is evaluated by a group of samples). The risk-seeking policy gradient formulation aims to increase the reward of the top  $\epsilon$  fraction of samples from the distribution, without regard for samples below that threshold. Therefore, this algorithm overcomes a performance bottleneck encountered in traditional policy gradient methods, enhancing its practical applications.

The update procedures to obtain best-fitted symbolic expressions can be summarized as shown in Algorithm 1. A brief introduction about the LSTM neural network and the RL algorithm is provided in appendixes A and B. For complete details about the DSR algorithm, the reader is invited to consult the original works by Petersen *et al.*<sup>20</sup>.

## 2. DSR for turbulence model development

Rather than recovering exact physical models from data, in the context of this work, the DSR method is employed to identify turbulence closures by searching over the space of tractable mathematical expressions to best fit the dataset from high-fidelity flow simulations. The theoretical foundation for this framework is the stress tensor decomposition proposed by Pope<sup>7</sup>. Taking the turbulent kinetic energy  $k$  and turbulence dissipation rate  $\epsilon$  as two scaling parameters, the Reynolds stresses and the rates of strain can be normalized as follows

$$\mathbf{b} = \boldsymbol{\tau}/k - \frac{2}{3}\mathbf{I}, \quad (10)$$

$$\mathbf{S} = \frac{1}{2} \frac{k}{\epsilon} [\nabla \mathbf{u} + (\nabla \mathbf{u})^T], \quad \mathbf{R} = \frac{1}{2} \frac{k}{\epsilon} [\nabla \mathbf{u} - (\nabla \mathbf{u})^T], \quad (11)$$

where  $\mathbf{I}$  is identity matrix,  $(\cdot)^T$  denotes matrix transposition.

It is postulated that  $\mathbf{S}$  and  $\mathbf{R}$  contain all information for determining  $\mathbf{b}$  and any tensor can be expressed by an infinite tensor polynomial. Leveraging the Cayley-Hamilton theorem, Pope proved that the normalized Reynolds stress tensor can be expressed as a finite polynomial linearly composed of tensor bases and scaler functions

$$\mathbf{b}(\mathbf{S}, \mathbf{R}) = \sum_m G^m(I_1, \dots, I_n) \mathbf{T}^m, \quad (12)$$

where  $G^m$  are several scalar coefficients determined by the invariants  $I_n$ , and  $\mathbf{T}^m$  are independent, symmetric tensor basis functions. For statistically two-dimensional flows, as is the case in present work, the coefficients are merely dependent on at most two invariants (i.e.,  $n = 2$ ) and the bases can be simplified to only three tensors (i.e.,  $m = 3$ ), as shown below

$$\mathbf{T}^1 = \mathbf{S}, \quad \mathbf{T}^2 = \mathbf{SR} - \mathbf{RS}, \quad \mathbf{T}^3 = \mathbf{S}^2 - \frac{1}{3}\mathbf{I} \cdot \text{Tr}(\mathbf{S}^2), \quad (13)$$

**Algorithm 1:** Symbolic regression based on reinforcement learning**Input:** learning rate  $\alpha$ ; entropy coefficient  $\lambda_{\mathcal{H}}$ ; risk factor  $\varepsilon$ ; batch size  $N$ ; reward function  $R$ .**Goal:** A symbolic mathematical expression that can best fit the dataset.**Initialize:** LSTM neural network with parameters  $\theta$ , defining distribution over expression  $p(\cdot | \theta)$ .**For** each epoch **do**

- 1:  $\mathcal{T} \leftarrow \left\{ \tau^{(i)} \sim p(\cdot | \theta) \right\}_{i=1}^N$  Sample  $N$  expressions
- 2:  $\mathcal{T} \leftarrow \left\{ \text{OptimizeConstants}(\tau^{(i)}, R) \right\}_{i=1}^N$  Optimize constants w.r.t. reward function
- 3:  $\mathcal{R} \leftarrow \left\{ R(\tau^{(i)}) \right\}_{i=1}^N$  Compute rewards
- 4:  $\mathcal{R}_\varepsilon \leftarrow \{(1 - \varepsilon)\text{-quantile of } \mathcal{R}\}$  Compute reward threshold
- 5:  $\mathcal{T} \leftarrow \left\{ \tau^{(i)} : R(\tau^{(i)}) \geq \mathcal{R}_\varepsilon \right\}$  Select subset of expressions above threshold
- 6:  $\mathcal{R} \leftarrow \left\{ R(\tau^{(i)}) : R(\tau^{(i)}) \geq \mathcal{R}_\varepsilon \right\}$  Select corresponding subset of rewards
- 7:  $\hat{g}_1 \leftarrow \text{ReduceMean}((\mathcal{R} - \mathcal{R}_\varepsilon) \nabla_\theta \log p(\mathcal{T} | \theta))$  Compute risk-seeking policy gradient
- 8:  $\hat{g}_2 \leftarrow \text{ReduceMean}(\lambda_{\mathcal{H}} \nabla_\theta \mathcal{H}(\mathcal{T} | \theta))$  Compute entropy gradient
- 9:  $\theta \leftarrow \theta + \alpha(\hat{g}_1 + \hat{g}_2)$  Apply gradients
- 10: **If**  $\max \mathcal{R} > R(\tau^*)$  **then**  $\tau^* \leftarrow \tau^{(\arg \max \mathcal{R})}$  Update best expression

**End****Return**  $\tau^*$ 

$$I_1 = \text{Tr}(\mathbf{S}^2), \quad I_2 = \text{Tr}(\mathbf{R}^2), \quad (14)$$

where  $\text{Tr}(\cdot)$  denotes the trace of matrix.

The utilization of invariants and tensor basis functions is the key to keep the Galilean and rotational invariance of turbulence model<sup>10</sup>. More generally, Embedding the invariance into the input features could better improve the model performance, which has been highlighted by some early works<sup>43,44</sup>. In the present work, the DSR approach is utilized to generate symbolic expressions for the coefficients, given the invariants and tensor bases. A simplified overview of the DSR framework used in present study is schematically depicted in Fig. 3. Since the flow simulations in present work are statistically in two dimensions, the input tokens are composed of two invariants and several other constants and mathematical operators. The three mathematical expressions produced by DSR correspond to the scalar coefficients  $G^1$ ,  $G^2$ , and  $G^3$ , respectively. The Reynolds stress can then be represented by the linear combination of mathematical expressions and tensor bases. The discrepancy between the Reynolds stress calculated by symbolic expressions and that from high-fidelity simulations is taken as the reward signal to inform the training process so as to maximize the performance of best-fitting expressions.

As is indicated in Fig. 3, however, only the non-linear part of Reynolds stress will be built by the developed framework. More specifically, instead of taking  $\mathbf{b}$  directly as the modeling subject, the deviatoric Reynolds stress is split into two portions as expressed by

$$\begin{aligned} \mathbf{b} &= \mathbf{b}^{\parallel} + \mathbf{b}^{\perp} \\ &= -2C_\mu \mathbf{S} + \mathbf{b}^{\perp}, \end{aligned} \quad (15)$$

where  $\mathbf{b}^{\parallel}$  and  $\mathbf{b}^{\perp}$  denote the linear and non-linear parts of Reynolds stress, respectively. Recalling that the standard  $k - \varepsilon$  turbulence model is used as the starting point for building data-driven models, the constant parameter  $C_\mu$  belonging to  $k - \varepsilon$  turbulence model (see Eq. 8) is kept in the linear portion.

This linear part will be taken as classical LEVM and solved implicitly in modified RANS solvers. As a consequence, the framework presented in Fig. 3 can be accordingly expressed in mathematics as

$$\mathbf{b}^{\perp} = \sum_{m=1}^3 G^m(I_1, I_2) \mathbf{T}^m, \quad (16)$$

where coefficients  $G$  will be represented by symbolic expressions consisting of invariants, constants and mathematical operators. In other words, only the non-linear portion of the Reynolds stress tensor,  $\mathbf{b}^{\perp}$ , will be predicted by the data-driven turbulence model.

This strategy aligns with the stability and accuracy analysis of data-driven turbulence models. In some earlier works<sup>10,45</sup>, the predictions from ML models are directly injected into RANS solvers. The remaining flow quantities are subsequently propagated forward by solving RANS equations with a frozen Reynolds stress field. Although prior assessments show that the discrepancy between ML predictions and high-fidelity data is pretty small, other derived flow variables of ultimate interest, such as velocity and pressure, are possibly far removed from the true values for flows with higher Reynolds numbers. Recently, a few studies<sup>46,47</sup> showed that embedding ML prediction, i.e. the Reynolds stress field, explicitly into RANS equations would inevitably result in the lack of accuracy of data-driven turbulence models. The minor error in predicted Reynolds stress would be significantly magnified during the forward iterations of RANS equations, thus leading to severe performance degeneration of data-driven RANS simulations. To avoid being ill-conditioned, it is necessary to decompose the Reynolds stress before it is injected into RANS simulations, as is done herein. This strategy has been proven to be effective in improving the stability and accuracy of data-driven RANS simulations<sup>19,46,47</sup>.

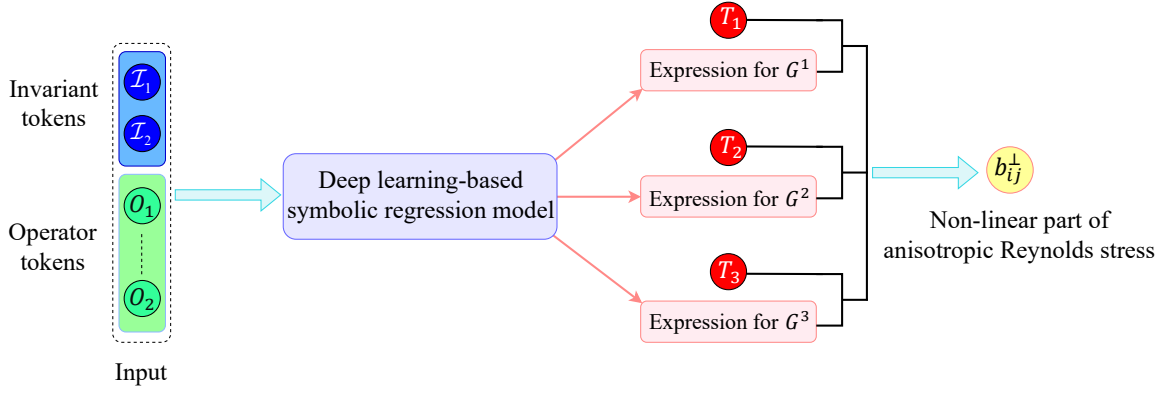


FIG. 3. Illustration of the DSR framework utilized in present work for building data-driven turbulence closures.

#### D. Numerical setup

All simulations in the present works are taken by the open-source CFD platform OpenFOAM<sup>48</sup>. The data-driven simulations can be divided into two rounds. In the first round, the baseline RANS simulation is performed by using the semi-implicit method for pressure-linked equations (SIMPLE) algorithm to achieve a converged solution. In the second round, a modified solver based on SIMPLE algorithm accepts the newly corrected non-linear part of the anisotropic Reynolds stress field. These corrections are then injected into RANS equations and iteratively solved until the residual reconverges. It should be emphasized that the turbulence closure consisting of symbolic expressions is only called once before the second round simulation starts, which means the predicted  $\mathbf{b}^\perp$  (non-linear part of anisotropic Reynolds stress tensor) is kept constant during the iteration of RANS equations.

For discretizing the RANS equations, the second-order central difference scheme is chosen for all terms except for the convection term, for which the second-order upwind scheme is selected. For all flow cases, the mesh independence experiment is first carried out before iteration starts, and all meshes are non-uniform with increased resolution around the feature of interest.

#### E. Summary of proposed approach

The entire procedures for implementing the data-driven turbulence model framework based on deep learning-based symbolic regression can be summarized as follows

1. Obtain the training dataset consisting of baseline RANS and DNS simulation data pairs. And run baseline RANS simulations for the testing flow set using the standard  $k - \varepsilon$  turbulence model (the baseline RANS solution will serve as the initial state for second round simulation evolved with symbolic predictions).
2. Obtain the input features from the training flow set, i.e., the invariants  $I_n$  and tensor basis functions  $\mathbf{T}^m$  from baseline RANS solutions.

3. Interpolate the DNS results to the RANS computational grids and then obtain the non-linear part of anisotropic Reynolds stress tensor (training target), i.e.,  $\mathbf{b}^\perp$ .
4. Construct the mapping function  $g : \omega_i(\mathbf{S}, \mathbf{R}) \mapsto \mathbf{b}^\perp$  by DSR approach. The hyperparameters are carefully tuned before they are applied to the training.
5. Integrate the symbolic expressed with simulation code. Replace the Reynolds stress term in the RANS solver with  $-2C_\mu \mathbf{S} + \mathbf{b}^\perp$ , and then run a forward simulation until residual re-converges. As aforementioned, the loose coupling strategy (the symbolic predictions are only called once) is adopted in this work. So the non-linear part  $\mathbf{b}_*^\perp$  is frozen while the linear part  $-2C_\mu \mathbf{S}$  is iteratively updated during the data-driven simulation.

### III. RESULTS

In this section, different flow configurations are investigated to verify the method proposed in this work. These flows are characterized by massive separations, which are difficult for traditional RANS turbulence models to perform accurate predictions. The corrected Reynolds stress tensor is substituted into the solver to obtain an improved mean flow field. The computation framework is verified by comparing the reconverged flow field with the high-fidelity mean flow, presenting a generalization performance on massively varying geometries.

#### A. Case setup for training and testing dataset

To assess the performance of the proposed framework, the classical cases of flow over parameterized periodic hills are selected, as shown in Fig. 4 (a). The left and right sides are connected to achieve periodicity. Hence, the cyclic boundary conditions are used at the inlet (left side) and outlet (right side). The geometries and DNS results are provided by Xiao *et al.*<sup>49</sup>. A parameter  $\alpha$  is utilized to change the hill steepness and the overall length of the geometry. The shape parameters for these three cases correspond to  $\alpha = 0.8, 0.5,$  and  $1.0$ , respectively.

The former is used as a training dataset. The obtained symbolic expression for turbulence closure is further applied to the latter two cases. In addition, the flow through a backward-facing step, which is significantly different from training data in geometry, is also selected to test the scope of application of the learned model, as shown in Fig. 4 (b). The geometry, DNS results, and experimental data are obtained from the works of Jovic and Driver<sup>50</sup> and Le, MOIN, and KIM<sup>51</sup>. For this backward-facing step case, A fixed velocity condition is enforced at the inlet, and a zero gradient condition is applied for the outflow. The no-slip boundary condition is applied at the top and bottom walls for all flow cases.

Other information about the training and testing cases, such as Reynolds number and Iterative steps for achieving convergence (residual of streamwise velocity is around  $1 \cdot 10^{-10}$ ), are summarized in Tab. I. A typical mesh description of periodic hill with  $\alpha = 0.8$  is presented in Fig. 5. The computational time may vary with hardware, but the simulation should achieve proper convergence performance within hundreds of seconds on a modern multi-core workstation. Additionally, it is noted that the converge cost with discovered turbulence model is basically the same with  $k - \varepsilon$  computation cost, as has been reported by previous studies<sup>9</sup>.

## B. Turbulence closure discovery

The traditional RANS turbulence models share a common weakness in correctly predicting the Reynolds stress anisotropy, which is blamed for the poor accuracy in many RANS-based flow simulations, especially in those with strong flow separations. As previously mentioned, a RL algorithm, known as the risk-seeking policy gradient algorithm, is employed to train the neural network. The non-linear part of anisotropic Reynolds stress tensor is set as the training target. As a consequence, taking the root-mean-square-error function, the reward function of DSR approach is accordingly defined as

$$\frac{1}{1 + \frac{1}{\sigma} \sqrt{\frac{1}{n} \sum_{i=1}^n \|\widehat{\mathbf{b}}_i^\perp - \mathbf{b}_i^\perp\|^2}}, \quad (17)$$

where  $\widehat{\mathbf{b}}^\perp$  is the true value of the non-linear part of anisotropic Reynolds stress tensor obtained from DNS results and  $\mathbf{b}^\perp$  is the corresponding prediction by symbolic expressions.  $n$  corresponds to the size of training dataset.  $\sigma$  denotes the standard deviation of  $\widehat{\mathbf{b}}^\perp$ . Here, the root-mean-square-error function is normalized by  $\sigma$  and is squashed to bound the range of reward value to (0, 1].

The main hyper-parameters used for symbolic training are listed in Tab. II, and the reward curve is illustrated in Fig. 6, as a function of total expressions evaluated during training. The tokens used to build symbolic expressions contain four regular arithmetic mathematical operators (+, -,  $\times$ ,  $\div$ ), constants, and input variables (i.e., the invariants). These tokens are selected to offer a compromise between the readability of the turbulence closure equation and prediction accuracy. Using non-linear

functions such as sin and tan could slightly improve the accuracy of DSR results, but the obtained expressions may be extremely complex. In addition, the computational cost could also be largely increased. Using the present configurations, the training takes about 100 hours on a workstation with 20 processor cores (Intel Xeon CPU E5-2650).

The goal of training efforts is to determine the mathematical expressions of scalar coefficients  $G^m(I_1, I_2)$ . To improve the training efficiency, the input invariants to the neural network are re-scaled by a sigmoidal function due to their strong varying in magnitude

$$\widehat{I}_i = \frac{1 - e^{-I_i}}{1 + e^{-I_i}}. \quad (18)$$

This operation consequently normalizes the input data to the range [-1, 1], thus reducing the negative impact of some possible outliers on the model performance. Without causing ambiguity, the symbol  $\widehat{(\cdot)}$  of normalized quantities are briefly dropped in the remainder of this work.

As indicated in Algorithm 1, the constant placeholders in sampled expressions need to be optimized to maximize the reward function. In this work, a non-linear optimization algorithm, known as Broyden-Fletcher-Goldfarb-Shanno (BFGS) algorithm<sup>52</sup>, is leveraged to substitute the constant placeholders with optimized constants. Since running constant optimization can be prohibitively expensive, the number of constant placeholders in each expression is limited to 3 during training.

The learned model takes the form ( $\beta = 7$ )

$$\mathbf{b}^\perp = \frac{\beta}{10} (G^1 \mathbf{T}^1 + G^2 \mathbf{T}^2 + G^3 \mathbf{T}^3), \quad (19)$$

where

$$\left. \begin{aligned} G^1 &= 0.1893I_1 + 0.2229I_2 + 0.1176 \\ G^2 &= -0.1036I_1I_2^3 - 0.05182I_1^2I_2^2 + 0.1718I_1^2 - 0.2333 \\ G^3 &= -2.514I_1I_2^4 - 3.514I_2^3 - 0.01105I_2^2 - 2I_1I_2 + 2.98I_2 \end{aligned} \right\}. \quad (20)$$

In this learned expression for  $\mathbf{b}^\perp$  (Eq. 19), the damping factor  $\beta/10$  is selected following the suggestion by Shih<sup>53</sup>. While a detailed discussion can be found therein, this factor is leveraged to ensure realizability conditions of the Reynolds stress tensor. A similar strategy was also utilized by Beetham and Capecelatro<sup>19</sup>. As is indicated by Eq. 20, the scalar coefficient expression multiplying by a higher-order basis tensor exhibits a much more complex form than the expression multiplying by a low-order basis as the former contains more high-order invariants. This result implies that the higher-order terms could yield relatively complex qualitative behavior in turbulent flow simulations. In addition, the coefficient expressions are functions of the invariants herein. By contrast, the turbulence closure models discovered by some other approaches, such as sparse regression and fast function extraction, only contain constant coefficients that keep unchanged for the whole computational domain. As a consequence, the method proposed in this work shows a degree of superiority since the coefficients vary with the invariants at different grid points, which tends to produce a more robust closure model.

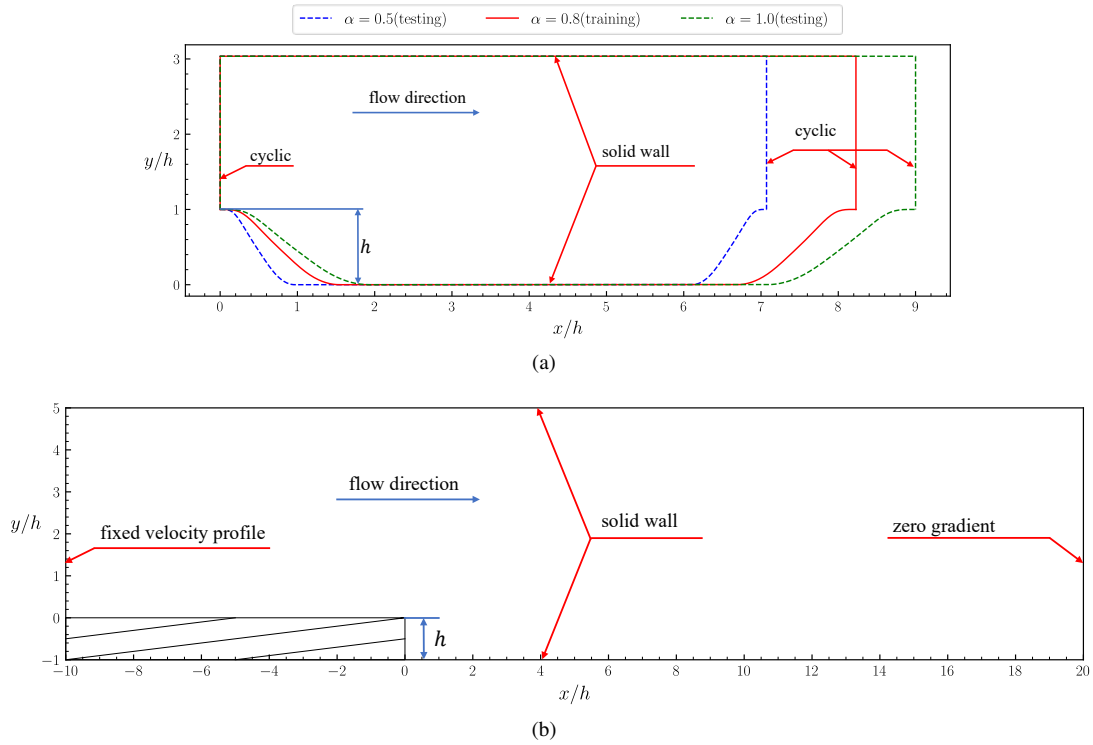


FIG. 4. Schematic of the geometries of (a) periodic hills and (b) backward-facing step.

TABLE I. Summary of flow cases used for training and testing.

Case use	Description	Cell number	Reynolds number	Characteristic length $h$	Iterative steps
Train	Periodic hill with $\alpha = 0.8$	Around 9600	5600	Hill height	20000
Test	Periodic hill with $\alpha = 0.5$	Around 9600	5600	Hill height	20000
Test	Periodic hill with $\alpha = 1.0$	Around 9600	5600	Hill height	20000
Test	Backward-facing step	Around 46000	5000	Step height	20000

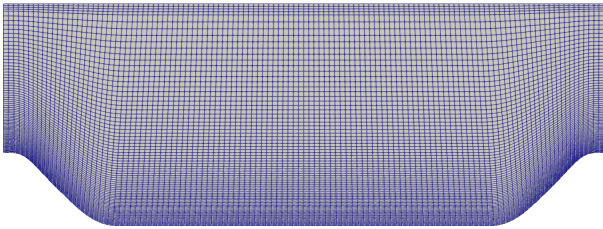


FIG. 5. Computation mesh of the periodic hill with  $\alpha = 0.8$ .

### C. Predictive results

The discovered model is first validated *a priori* for the training periodic hill flow case ( $\alpha = 0.8$ ). Within this effort, the accuracy of the learned model is evaluated by high-fidelity data based on the predicted anisotropic Reynolds stress tensor. In

TABLE II. Main DSR hyper-parameters used for searching symbolic expressions of turbulence closures.

LSTM architecture (3 hidden layers)	64 $\rightarrow$ 64 $\rightarrow$ 64
Train epochs	20
Batch size	640
Learning rate	0.001
Entropy coefficient	0.005
Risk factor	0.05
Minimum length of expressions	4
Maximum length of expressions	32
Mathematical operators	[+, -, $\times$ , $\div$ ]
Constant token repeats	3

the following context, the unnormalized anisotropic Reynolds stress tensor  $\mathbf{a} = k \cdot \mathbf{b}(\mathbf{S}, \mathbf{R})$  will be referred to as the tensor used for solving RANS equations.

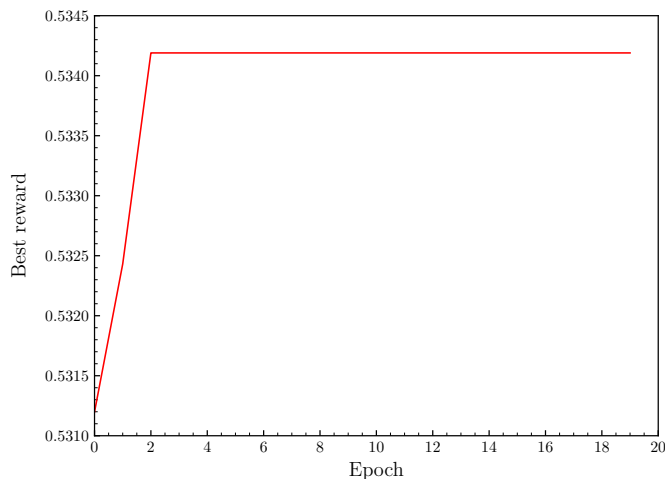


FIG. 6. Reward training curve for using DSR to discover turbulence closure models. The curve shows the best reward value as a function of total expressions evaluated so far.

As is presented in Fig. 7, the baseline RANS simulation provides a reasonably good prediction for shear component  $a_{12}$ , even though some over-predictions can be observed at the downstream crest. However, its predictions for other three diagonal components are far removed from high-fidelity DNS observations. Such inaccuracy is more obvious for  $a_{22}$  and  $a_{33}$ , of which the prediction bias is particularly stark near the bottom wall. By contrast, the learned model captures the correct sign and presents a higher precision in the magnitude for all components of the anisotropic Reynolds stress tensor. Although the improvement can be plagued at certain flow areas, the discovered model generally provides better predictions than LEVM. This superiority is relatively more significant for  $a_{11}$  and  $a_{22}$  in the region where flow separations could exist. The last two rows in Fig. 7 demonstrate the discrepancy between the highly-resolved DNS data and the results obtained from LEVM and the learned model, respectively. It indicates that the learned model is, to some extent, more capable to reduce the predictive error in the anisotropic stress tensor.

As aforementioned, the independent basis tensors and invariants representing key turbulence features are leveraged during the training process to guarantee both Galilean and rotational invariance of the discovered model. To make a deeper investigation into the realizability of the discovered turbulence model, the barycentric map<sup>54</sup> based on the combination of eigenvalues is used to provide a non-distorted visual representation of the turbulence anisotropy. The anisotropic Reynolds stress tensor predicted by the discovered symbolic model is shown in Fig. 8, compared with baseline RANS and DNS results. The comparisons are performed on six streamwise locations at  $x/h = 1.5$ ,  $x/h = 1.0$ ,  $x/h = 1.5$ ,  $x/h = 2.0$ ,  $x/h = 4.0$  and  $x/h = 7.5$ , respectively. As indicated in Fig. 8, the Reynolds stress anisotropy approaches the three-component limiting state for all three models as the point moves away from the bottom wall. This trend can ascribe to the significantly fewer flow separations in the bulk region, thus the turbulence gradually de-

velops to be isotropic. It is also noted that the baseline RANS Reynolds stress is close to the plane-strain limiting state at all six locations, showing significant discrepancies from the DNS results. The baseline RANS flow field is generally dominated by the shear layer, thus the medium eigenvalue of baseline RANS stress anisotropy is close to zero<sup>54</sup>. By contrast, the discovered model is more capable to capture the stress anisotropy to achieve better agreement with DNS data, even though there are a tiny minority of outliers as shown in Fig. 8 (c). It is worth stressing that these few outliers could hardly impede the performance of the learned model, as is discussed in the following context.

The improved velocity and pressure fields, compared with the DNS data and the results obtained via standard  $k - \epsilon$  model, are shown in Fig. 9 (both tow fields are non-dimensional). The streamline resulting from DNS data in Fig. 9 (a) shows that the baseline RANS model underestimates the size of separation bubble, revealing that the standard  $k - \epsilon$  model is not capable of precisely capturing the flow separation feature for this case. The learned model provides more accurate Reynolds stress anisotropy. Therefore, it successfully enlarges the RANS-predicted separation bubble. An analogous improvement is also reflected by the magnitude of pressure in Fig. 9 (b). The baseline RANS model over-predicts the pressure magnitude at the upstream and downstream hillcrest. In addition, it also under-predicts the pressure at the downstream bulk region. By contrast, the result predicted by the discovered model is more consistent with DNS data. The advantage of the discovered model is more specifically demonstrated by the velocity and pressure differences. At the upstream hillcrest where flow separation happens, the relative error of baseline RANS results to DNS results is nearly double larger than the error of learned flow fields to corresponding DNS flow fields.

An additional quantitative investigation into the prediction performance of the learned model is described in Fig. 10, in which the predictive velocity profiles are compared against DNS data. The result of the baseline RANS method shows a large departure from the DNS result. As a comparison, the velocity profiles predicted via the discovered model demonstrate remarkable improvement over traditional RANS-based results in the whole flow region.

By reviewing the RANS governing equation for momentum (Eq. 2), it is straightforward to deduce that the difficulty inherent in calculating the anisotropic Reynolds stress components  $a_{11}$  and/or  $a_{12}$  (note that the flow is two-dimensional) is perhaps the major contributing factor for the incapacity to accurately predict flow separations with traditional turbulence models. As can be seen in Fig. 7, while the standard  $k - \epsilon$  turbulence model generally makes good predictions for shear component  $a_{12}$ , it cannot capture the right sign and magnitude of normal component  $a_{11}$ . The learned model provides relatively better predictions for these two tensor components. Although the flow past the periodic hill is generally dominated by the shear layer (especially at the region where flow separation occurs), the deficiency in Reynolds stress anisotropy impairs the performance of  $k - \epsilon$  turbulence model, rendering the predictions for other quantities of interest, such as velocity and pressure, inaccurate. To further investigate how the

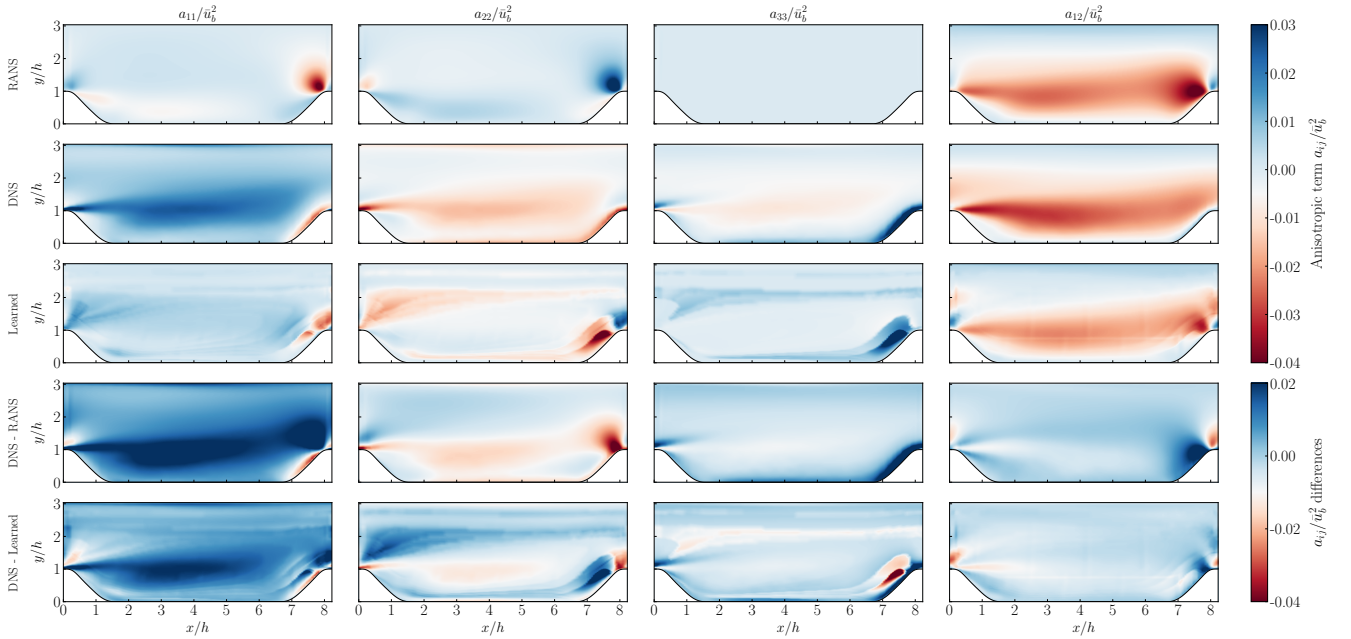


FIG. 7. Comparison of anisotropic Reynolds stress components for periodic hill training flow ( $\alpha = 0.8$ ) using LEVM, DNS, and the learned model, respectively. From left to right:  $a_{11}$ ,  $a_{22}$ ,  $a_{33}$ , and  $a_{12}$ . From top to bottom: baseline RANS solutions, time-averaged DNS solutions, the learned model solutions, and the difference between exact data and predicted data by LEVM and the learned model, respectively. All results are normalized by the bulk velocity at crest  $\bar{u}_b$ .

symbolic model contributes to the flow simulation, the contributions from the tensor basis functions consisting of the learned model  $\mathbf{b}^\perp$  as well as the iteratively updated linear part  $\mathbf{b}^\parallel$  are presented in Fig. 11. It can be observed that the linear part  $\mathbf{b}^\parallel$  and the first tensor basis  $\mathbf{T}^1$  dominate the calculation for  $a_{12}$ , and the second tensor basis  $\mathbf{T}^2$  is the most important contributor for describing  $a_{11}$ . Thus the linear part and the first two bases are the most important ingredients for accurately capturing the flow separation. More precisely, it is their gradients that determine the calculation of the recirculation region since the momentum equation is solved with the divergence of Reynolds stress. The third tensor basis  $\mathbf{T}^3$  makes the most important contribution for modeling  $a_{33}$ , which enhances the anisotropic property of the predicted stress tensor.

#### D. Application beyond the training scope

It has been presented in Section III C that the model discovered with the present method shows promising improvements in the predictive accuracy of RANS-based simulations. To evaluate whether the learned model can achieve similar accuracy improvements for cases outside its training scope, the model in Eqs. 19 and 20 are applied to three test cases with different geometries, as shown in Fig. 4. As has been done in previous discussions, the performance of the learned model is assessed by comparing its predictions against the LEVM and high-fidelity data.

Although the geometrical configurations of the first two test cases are similar to that of the training case, the flow be-

haviors are highly susceptible to the varying hill slope and channel length. Figs. 12 and 13 present barycentric maps of the Reynolds stress anisotropy predicted by the learned model for these two periodic hill test flows with  $\alpha = 0.5$  and 1.0, respectively. For each test case, the Reynolds stress anisotropy at three typical streamwise locations, i.e., the upstream and downstream hill crests as well as the middle flat section, are selected to demonstrate the prediction performance of the learned model. Similar to the results shown in Fig. 8, the realizability condition for anisotropic Reynolds stress tensor is well-maintained by the learned model. In addition, it clearly shows that the anisotropy predictions at all three cross-sections are markedly improved, albeit not in complete accord with the DNS predictions.

Substituting the corrected Reynolds stress fields into the CFD solver, the velocity improvements over LEVM can be observed in Fig. 14 for the test cases. While the improvements are not distinguishable for case  $\alpha = 0.5$  at the recirculation region, the discovered model indeed makes contributions to improve the accuracy of flow separation prediction for case  $\alpha = 1.0$ . The observed inaccuracies in case  $\alpha = 0.5$  can be ascribed to its larger hill slope, thus the flow separation is more severe than that of the training case. Moreover, the learned model generally produces better predictions for both test cases at the bulk region. The improvements can also be quantitatively verified by comparing the overall prediction error in streamwise velocity. Figs. 15 presents the distribution of error in streamwise velocity when applying the learned model, compared with the corresponding results obtained by baseline simulations. For both test cases, it can be observed that the learned model provides a higher proportion of low relative error than the baseline

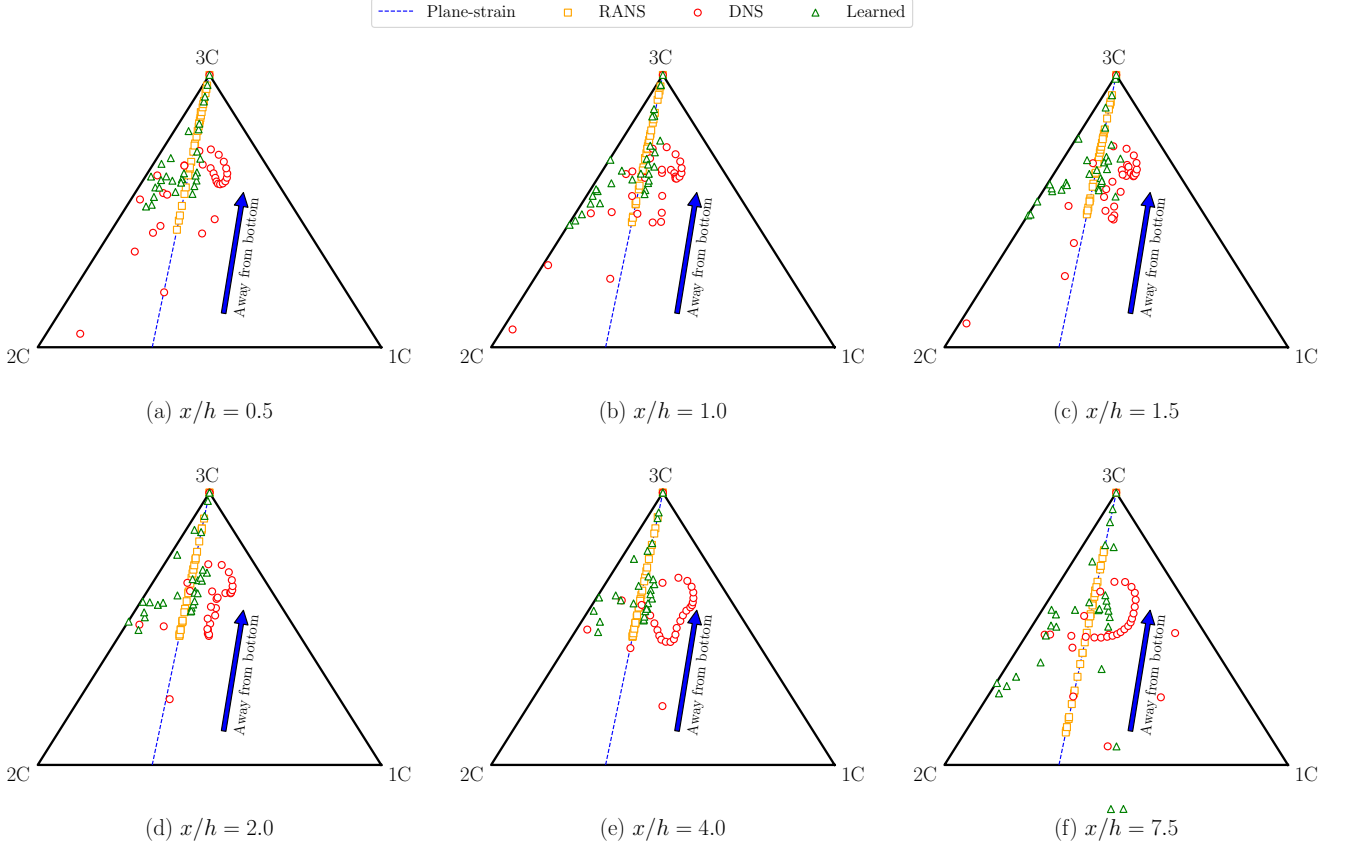


FIG. 8. Barycentric map of the predicted Reynolds stress anisotropy for periodic hill training flow ( $\alpha = 0.8$ ). The learned predictions on six streamwise locations at  $x/h = 0.5$ ,  $x/h = 1.0$ ,  $x/h = 1.5$ ,  $x/h = 2.0$ ,  $x/h = 4.0$  and  $x/h = 7.5$  are compared with the corresponding results from high-fidelity DNS simulations and the standard  $k - \varepsilon$  RANS turbulence model in (a)-(f), respectively.

turbulence model. As the relative error increases, the number of data points corresponding to the learned model quickly decreases. Despite the learned model could produce higher errors in part of the computational domain, it generally outperforms the baseline turbulence model.

The last test case considered here is turbulent flow over a backward-facing step at  $Re = 5000$ . Its geometry is far removed from the flow scenario under which the symbolic model is discovered. Thus this case would be a more comprehensive assessment of the generalization performance of the learned model. Since full-field data are not available for this flow configuration, the performance of discovered model is assessed by comparison with reported DNS data<sup>50</sup> and experimental data<sup>51</sup>. As expected in Fig. 16, the velocity profiles predicted by the learned model are much closer to high-fidelity velocity data across the whole domain (the figure is zoomed into the near-step region due to the limitation of available DNS and experiment data). It should be emphasized that the symbolic model is only trained on one flow through a periodic hill, but it still achieves promising improvements for out-of-scope flow configurations.

### E. Effect of reward functions

As introduced in Section II C 1, the deep symbolic regression method uses a RL algorithm to train the neural network, thus the choice of the reward function would have a direct effect on the final form of discovered models. The results discussed above are based on the model using a modified root-mean-square-error function (Eq. 17) as its reward function. In this section, another different reward function is utilized to investigate whether a different symbolic model can be discovered, and more importantly, whether similar accuracy improvements can be achieved by the new model.

The new reward function is constructed as

$$-\log\left(1 + \frac{1}{n} \sum_{i=1}^n \|\widehat{\mathbf{b}}_i^\perp - \mathbf{b}_i^\perp\|^2\right), \quad (21)$$

where  $n$ ,  $\mathbf{b}^\perp$  and  $\widehat{\mathbf{b}}^\perp$  keep the same as is in Eq. 17. Compared with Eq. 17, the root-mean-square-error is not normalized in this reward function. With the use of the logarithmic function, it would be expected that different closure models can be discovered.

Using the same training dataset (i.e., case  $\alpha = 0.8$  in Fig. 4 (a)) and parameters as listed in Tab. II, the discovered model

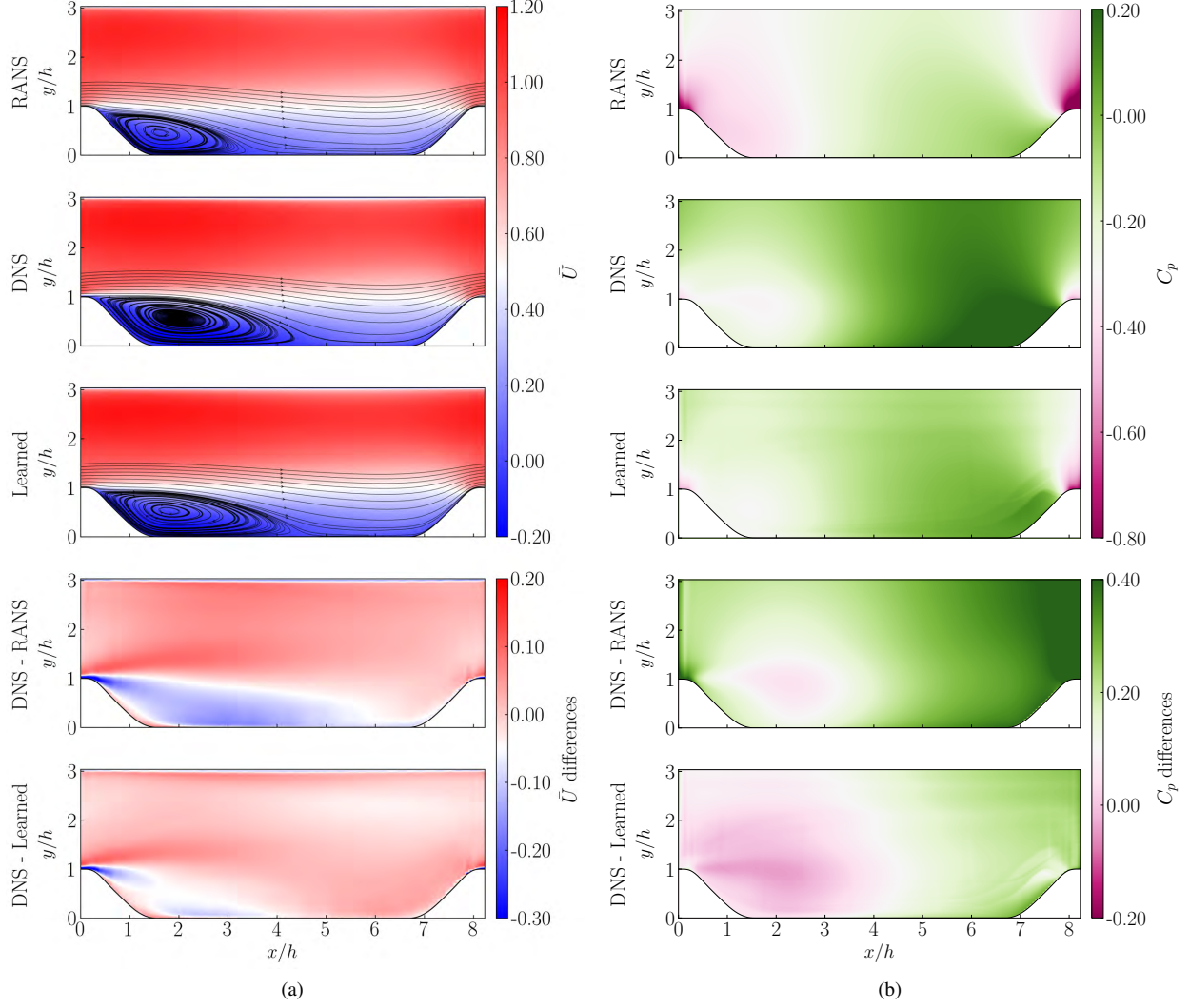


FIG. 9. Comparison of (a) normalized streamwise velocity  $\bar{U}$  and (b) pressure coefficient  $C_p$  for periodic hill training flow ( $\alpha = 0.8$ ) using LEVM, DNS, and the learned model, respectively. From top to bottom: baseline RANS solutions, time-averaged DNS solutions, the learned model solutions, and the difference between exact data and predicted data by LEVM and the learned model, respectively.

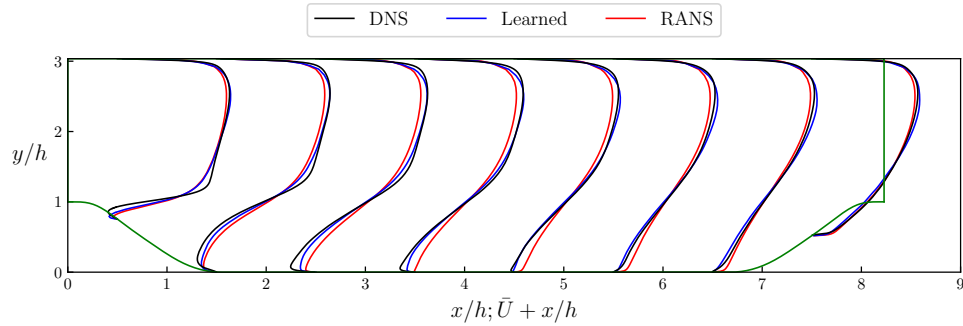


FIG. 10. Normalized streamwise velocity profiles from the learned symbolic model for periodic hill training flow ( $\alpha = 0.8$ ), in comparison with the DNS data as well as the baseline RANS results obtained via  $k - \epsilon$  model.

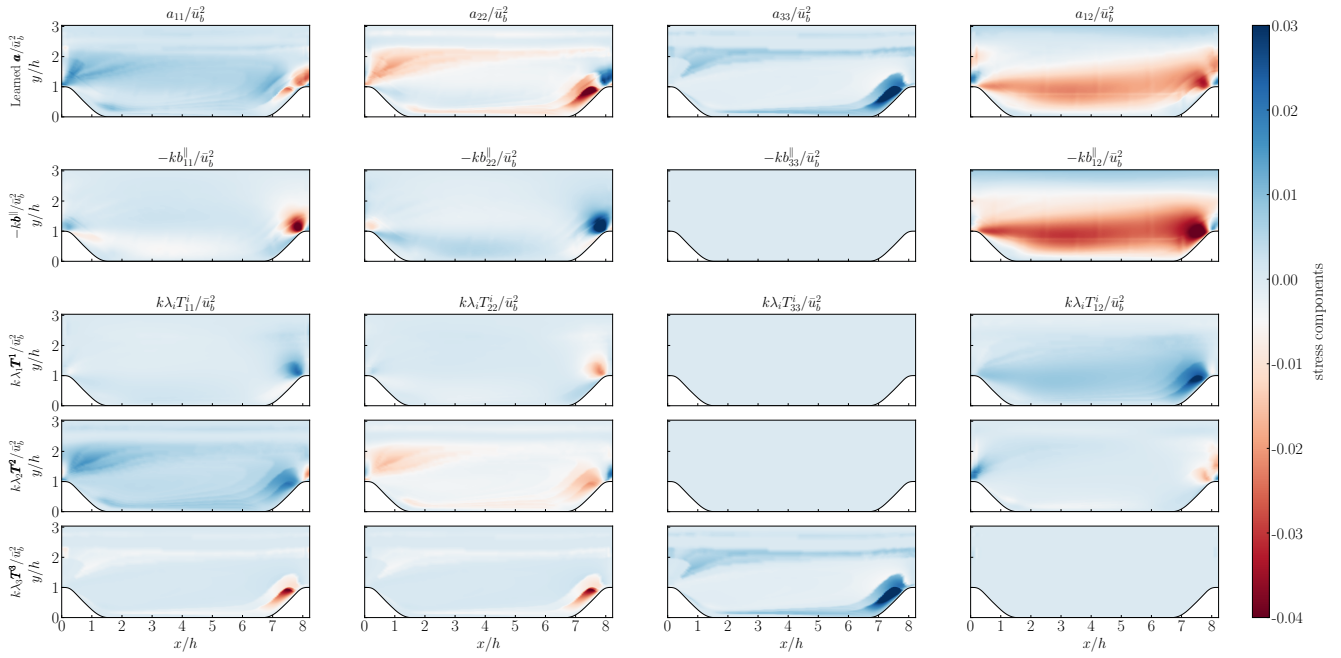


FIG. 11. Contribution to each component of the Reynolds stress anisotropy from each tensor basis for the learned model as well as the linear part. All results are normalized by the bulk velocity at crest  $\bar{u}_b$ .

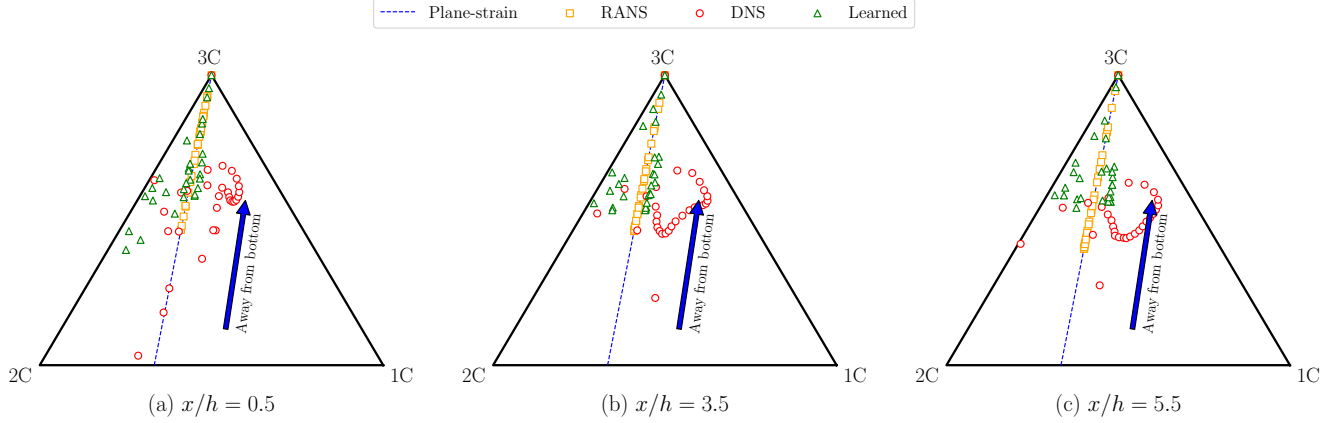


FIG. 12. Barycentric map of the predicted Reynolds stress anisotropy for periodic hill test flow ( $\alpha = 0.5$ ). The learned predictions on three streamwise locations at  $x/h = 0.5$ ,  $x/h = 3.5$ ,  $x/h = 5.5$  are compared with the corresponding results from high-fidelity DNS simulations and the standard  $k - \varepsilon$  RANS turbulence model in (a), (b) and (c), respectively.

by taking Eq. 21 as the reward function is

$$\begin{aligned} \mathbf{b}^{\perp} = \frac{\beta}{10} & [(0.8603I_1^2I_2^2 + 0.8603I_1^2I_2 + 0.3014I_1^2 + 0.7206I_1I_2 + 0.5144I_1)\mathbf{T}^1 \\ & + (0.5544I_1^2I_2^6 - 0.5544I_1^3I_2^4 - 0.06858I_1^2I_2^4 - 0.5544I_1I_2^2 - I_1I_2 - 0.3865)\mathbf{T}^2 \\ & + (-1.328I_1^3I_2^2 + 1.328I_1^2I_2^3 + I_1I_2^2 - 3.289I_1I_2 + 3I_2^2 + 4.624I_2)\mathbf{T}^3], \end{aligned} \quad (22)$$

where the damping factor  $\beta/10$  keeps the same value as in

Eq. 19. For simplifying the discussion in the following context,

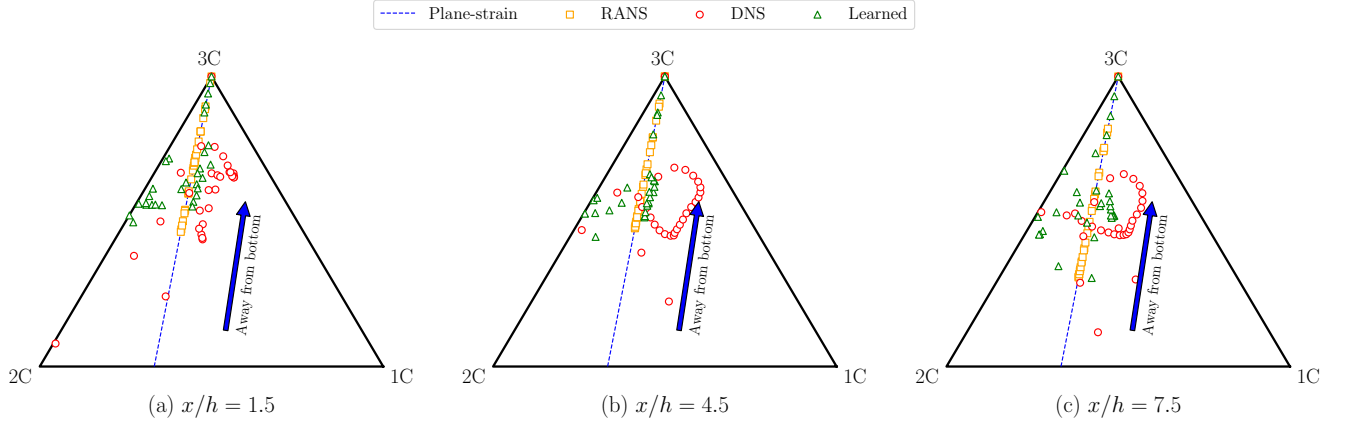


FIG. 13. Barycentric map of the predicted Reynolds stress anisotropy for periodic hill test flow ( $\alpha = 1.0$ ). The learned predictions on three streamwise locations at  $x/h = 1.5$ ,  $x/h = 4.5$ ,  $x/h = 7.5$  are compared with the corresponding results from high-fidelity DNS simulations and the standard  $k - \varepsilon$  RANS turbulence model in (a), (b) and (c), respectively.

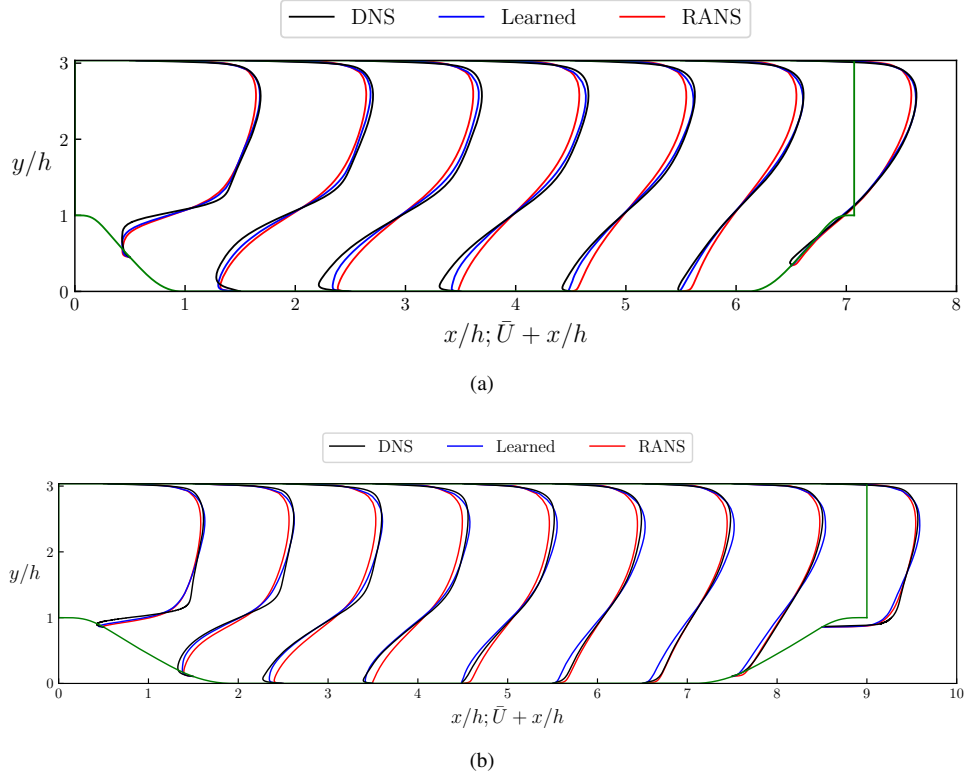


FIG. 14. Normalized streamwise velocity profiles from the learned symbolic model for two periodic hill test cases, in comparison with the DNS data as well as the baseline RANS results obtained via the standard  $k - \varepsilon$  model. (a)  $\alpha = 0.5$ , (b)  $\alpha = 1.0$

the two discovered models in Eqs. 20 and 22 are referred to as model 1 and model 2, respectively.

Comparing the two models discovered by different reward functions, the learned model 2 shows a more complex form, even though the training of both model 1 and model 2 is carried out using the same dataset and hyper-parameters. Specifically, for the scalar coefficient corresponding to the same tensor basis, the order of invariants in model 2 is much higher than

that in model 1, which means that there are more multiplying operations when applying model 2. By contrast, the higher-order terms, such as  $0.5544I_1^2I_2^6$ , fail to survive in the training evolution of model 1. On the other hand, it is noted that the symbolic expressions in model 1 contain fewer terms, resulting in a more compact form of turbulence closure model.

The next step is to investigate the performance of model 2. Even though model 2 presents a different functional form from

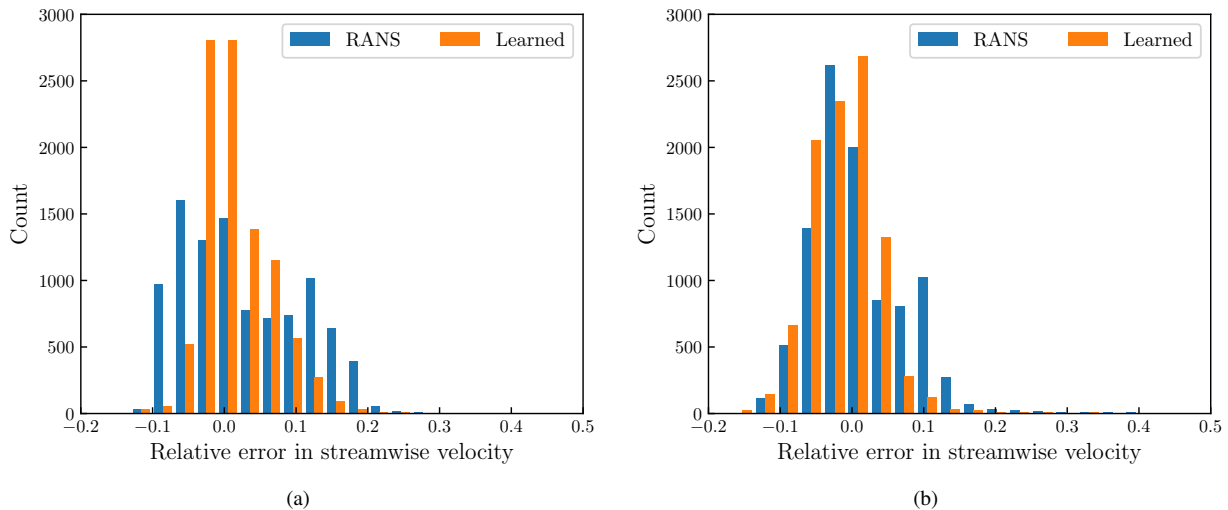


FIG. 15. Error distribution in normalized streamwise velocity for two periodic hill test cases. The relative error is calculated by  $U_p - U_{DNS}$ , where  $U_p$  is predicted by the learned model or the standard  $k - \epsilon$  model and  $U_{DNS}$  indicates the DNS velocity. (a)  $\alpha = 0.5$ , (b)  $\alpha = 1.0$ .

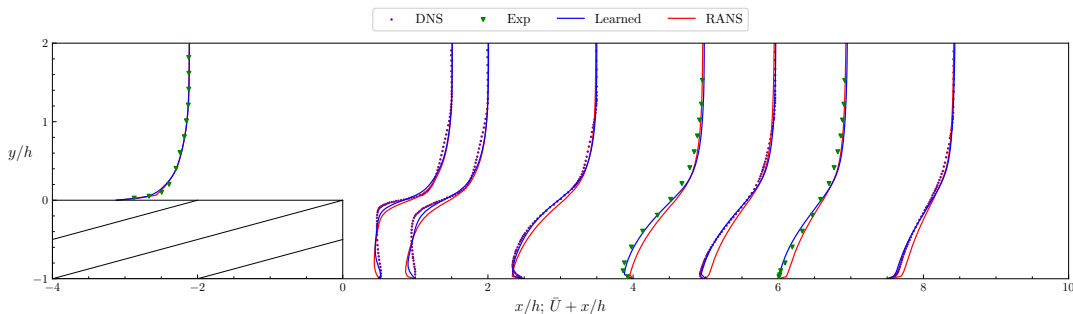


FIG. 16. Normalized streamwise velocity profiles (zoomed into the near-step region) from the learned symbolic model for backward-facing step test case, in comparison with the reported DNS data as well as the experiment data.

model 1, the use of a physics-based constraint of the tensor basis set could ensure that reasonable accuracy improvements can be achieved. For brevity, periodic hill cases  $\alpha = 0.5$  and  $\alpha = 0.8$  corresponding to the extrapolated test case and train case are selected to demonstrate the predictive performance of model 2, in comparison with the results obtained by model 1. As can be seen in Figs. 17 and 18, both the two discovered models can satisfy the realizability requirement. In a sense, model 2 performs even better than model 1 since there are no outliers in its predictions, as shown in 18 (c). In general, the two learned models outperform the baseline RANS turbulence model across the whole domain. Although model 2 has a more complex form, it has no distinct advantages over model 1 in improving the accuracy of Reynolds stress anisotropy.

Fig. 19 shows a comparison of streamwise velocity predicted by the two learned models. It is noted that the two discovered models result in strikingly close velocity fields, even though model 2 bears little resemblance to model 1. This scenario can be ascribed to the statistical error associated with velocity and Reynolds stress. Specifically, the mean velocity is a first-order statistic, whereas the Reynolds stress is a second-

order statistic that is less converged, as has been reported by Thompson *et al.*<sup>55</sup>. Compared with baseline RANS predictions, both two discovered models can achieve promising accuracy improvements for all flow cases, even if the corresponding configuration is outside the training scope.

#### IV. CONCLUSIONS

In this work, a data-driven RANS turbulence modeling approach based on the combination of deep learning and symbolic regression techniques is proposed. This approach leverages the representational capability of deep learning to search the symbolic space for generating interpretable expressions. A risk-seeking RL algorithm is leveraged to train the LSTM neural network so as to maximize the best sampled expressions. The resultant turbulence closures are explicitly given in the form of algebraic polynomials via the embedded invariants and tensor basis functions, thus allowing direct functional inference and achieving promising Galilean invariance properties. In addition, with the use of present method, it is straightforward

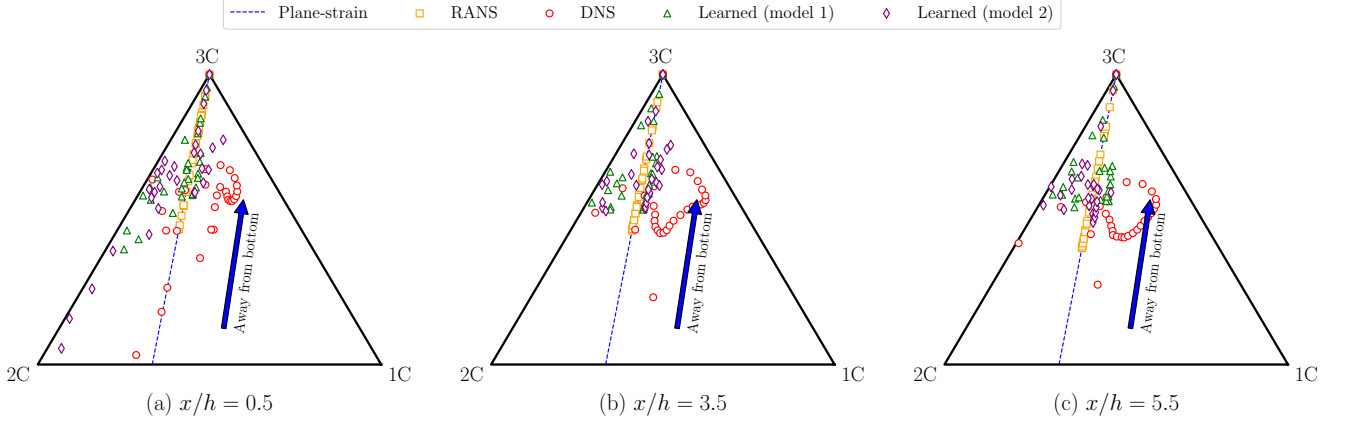


FIG. 17. Barycentric map of the Reynolds stress anisotropy predicted by learned model 2 (Eqs. 20) for periodic hill test case  $\alpha = 0.5$ , compared with the corresponding results from model 1 (Eqs. 22).

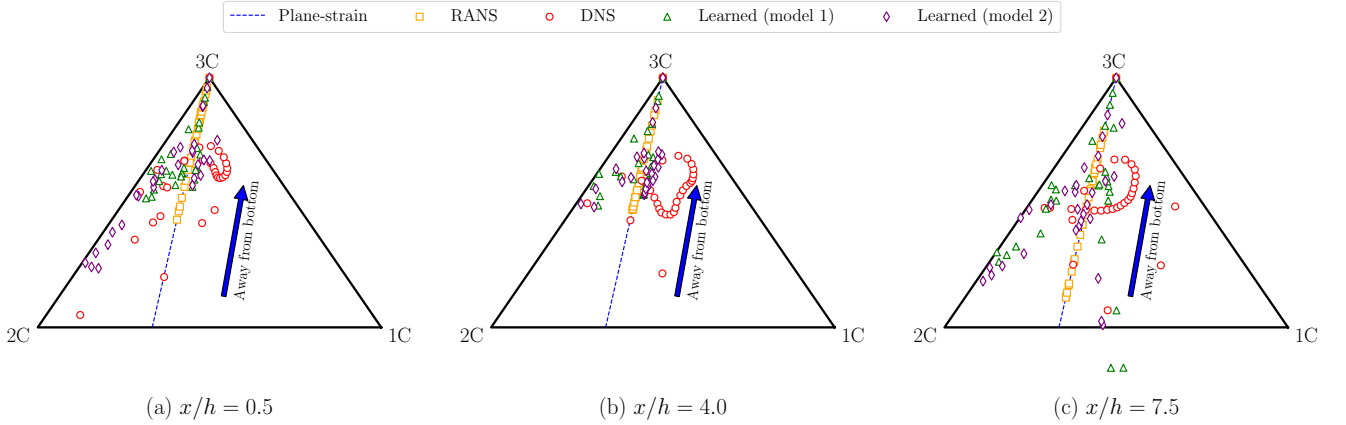


FIG. 18. Barycentric map of the Reynolds stress anisotropy predicted by learned model 2 (Eqs. 20) for periodic hill train case  $\alpha = 0.8$ , compared with the corresponding results from model 1 (Eqs. 22).

to implement the discovered model equations into existing RANS solvers, without the need to deploy a deep learning environment for new data-driven simulations.

The performance of the proposed approach is validated by three canonical flows that differ in geometrical configurations. Although the training dataset consists of only one flow through a periodically constricted channel, the learned turbulence model, on the whole, demonstrates promising accuracy improvements compared with LEVM for all test flows, even for extrapolated cases that could hold flow features not seen during the training process. The algebraic form renders the discovered model more realizable in practical RANS simulations. Additionally, the reward function plays an important role in discovering the symbolic turbulence model since the neural network is trained by RL algorithms. In the context of this study, two reward functions are employed. While the two discovered turbulence models differ greatly in function forms, their predictions show a certain degree of similarities, especially for the low-order statistics.

Despite the relative simplicity of the selected RANS simulations, the experience and insights gained from this work

shed a light on the future development of interpretable data-driven turbulence models. One of the most challenging issues is developing a reliable and interpretable model that can present universally good performance for complex industrial flow simulations. The model performance could be enslaved by the policy used in RL training<sup>37</sup>. Another issue is about the relatively high computation cost regarding the constant optimization in DSR method, or more generally, the training. Fuelled by the advances of symbolic regression methods and RL algorithms in ML community, it is anticipated that more comprehensive frameworks can be constructed for turbulence modeling research. By integrating the RANS simulations with RL-based training process, the reward can be defined by other quantities of interest, so that the discovered model would be more consistent with physical observations<sup>37</sup>. In addition, by extending RL with special types of neural networks, a non-local constitutive models could be developed for improving the performance of data-driven turbulence models<sup>40,56</sup>.

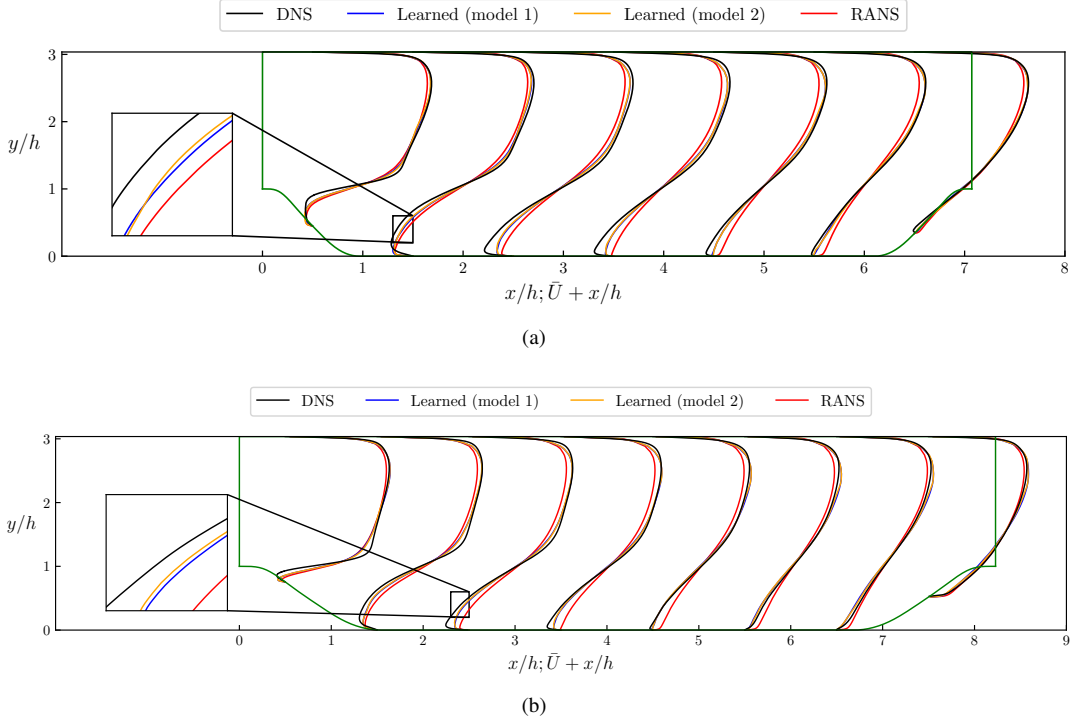


FIG. 19. Normalized streamwise velocity profiles obtained by using the learned model 2, in comparison with the corresponding results from model 1. (a) Periodic hill test case  $\alpha = 0.5$ ; (b) Periodic hill train case  $\alpha = 0.8$ .

## V. DATA AVAILABILITY

The relevant code and data used in this project are publicly available at <https://github.com/thw1021/DSRRANS>. The DSR method is implemented by Petersen *et al.*<sup>20</sup> using deep learning library TensorFlow<sup>57</sup>, and the CFD simulations are carried out by using OpenFOAM<sup>48</sup>.

## VI. ACKNOWLEDGEMENTS

This work is supported by the National Key Research and Development Program (Grant Nos. 2019YFE0192600 and 2019YFB1503700), Natural Science Foundation of China (Grant No. 52006098), and Priority Academic Program Development of Jiangsu Higher Education Institutions. Y. Wang acknowledges the support of the Natural Science Foundation of China (Grant Nos. 11902153 and 12272178), the Research Fund of State Key Laboratory of Mechanics and Control of Mechanical Structures (Grant No. MCMS-I-0122G01) and Key Laboratory of Computational Aerodynamics, AVIC Aerodynamics Research Institute.

### Appendix A: Brief overview of LSTM neural network

The LSTM network is a special variant of RNN. It is designed to process data sequences and utilizes its internal memory to learn and harness information relative to what it has seen

so far. As a consequence, the network predictions are not only determined by the current input but also conditionally dependent on the recent input sequence. A schematic of the LSTM network is shown in Fig. 20. A typical LSTM cell contains three gates: the input gate  $i$ , output gate  $o$  and forget gate  $f$ . The cell input and output are given by  $x$  and  $h$ , respectively.

Compared to the standard RNN, the LSTM network introduces an additional mechanism to carry information, i.e., the cell state  $c$ , across many timesteps. The basic equations involved in the forward computation of LSTM networks are given as follows

$$\begin{aligned}
 f_t &= \sigma(W_f \cdot [h_{t-1}, x_t] + b_f), \\
 i_t &= \sigma(W_i \cdot [h_{t-1}, x_t] + b_i), \\
 c'_t &= \tanh(W_c \cdot [h_{t-1}, x_t] + b_c), \\
 c_t &= f_t * c_{t-1} + i_t * c'_t, \\
 o_t &= \sigma(W_o \cdot [h_{t-1}, x_t] + b_o), \\
 h_t &= o_t * \tanh(c_t),
 \end{aligned} \tag{A1}$$

where  $\sigma$  is the sigmoid activation function,  $W$  and  $b$  are the weights and biases, respectively. As indicated in Fig 20, the cell state  $c$  is combined with the input connection and the recurrent connection, and it will work together with the three gates to affect the next cell state by adding or removing information. Conceptually, the carry dataflow keeps reading and writing from memory, thus allowing past information to be injected at a later time. This mechanism is the key ingredient that ensures the LSTM network does not suffer from vanishing or exploding gradients.

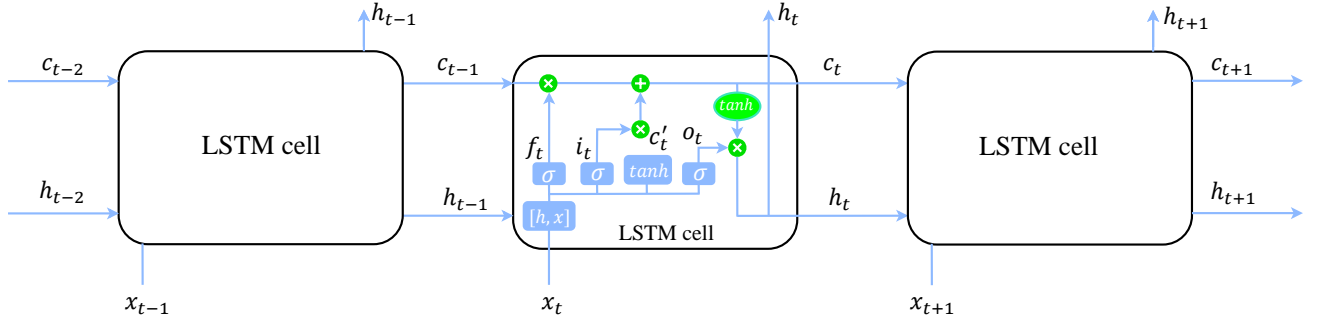


FIG. 20. Architecture of the LSTM network.

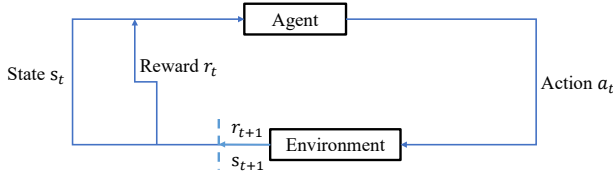


FIG. 21. A schematic of the RL framework.

## Appendix B: RL with the risk-seeking policy gradient algorithm

RL is one of the main branches of machine learning. It is concerned with how to learn through trial and error from environmental feedback so as to maximize a numerical reward signal. A simplified overview of the RL framework is presented in Fig. 21. As illustrated, there are two core components, the agent and environment, in RL. The environment represents the problem and the agent attempts to find the solution to the problem. In general, the learning agent interacts with the environment through three channels: the state, action and reward. The agent perceives the state of its environment and chooses actions to affect the environment. The environment then reacts to the actions by producing a reward signal. After finishing training, the agent is expected to perfectly map situations to actions so that the reward signal can be maximized.

In the present work, the risk-seeking policy gradient algorithm is employed to train the LSTM neural networks to produce better-fitting symbolic expressions. The core idea of the risk-seeking policy gradient can be expressed as

$$J(\theta; \varepsilon) = \mathbb{E}_{\tau \sim p(\tau|\theta)} [R(\tau) \geq R_\varepsilon(\theta)], \quad (\text{B1})$$

where  $R_\varepsilon(\theta)$  denotes the  $(1 - \varepsilon)$ -quantile of the reward distribution produced by the current policy. Therefore the learning objective  $J(\theta; \varepsilon)$  is to maximize the reward of the top  $\varepsilon$  fraction of samples. The samples below the threshold will not involve in the training process. This strategy has been proven to be instrumental in improving the performance of sampled symbolic expressions. In the context of this work, the distribution over mathematical expressions  $p(\tau | \theta)$  is like a policy. The algorithm agent samples new tokens when the parent and sibling inputs are observed. During every episode, the agent generates a sequence of expressions, and the reward value is

then calculated by the reward function.

- <sup>1</sup>D. J. Mavriplis, "Progress in computational fluid dynamics discretizations algorithms and solvers for aerodynamic flows," *AIAA Journal* **0**, 1–23 (2021).
- <sup>2</sup>D. C. Wilcox, *Turbulence modeling for CFD*, Vol. 2 (DCW industries La Canada, CA, 1998).
- <sup>3</sup>K. Duraisamy, G. Iaccarino, and H. Xiao, "Turbulence modeling in the age of data," *Annual Review of Fluid Mechanics* **51**, 357–377 (2019).
- <sup>4</sup>K. Duraisamy, "Perspectives on machine learning-augmented reynolds-averaged and large eddy simulation models of turbulence," *Phys. Rev. Fluids* **6**, 050504 (2021).
- <sup>5</sup>S. H. Cheung, T. A. Oliver, E. E. Prudencio, S. Prudhomme, and R. D. Moser, "Bayesian uncertainty analysis with applications to turbulence modeling," *Reliability Engineering & System Safety* **96**, 1137–1149 (2011).
- <sup>6</sup>C. Yan, Y. Zhang, and H. Chen, "Data augmented turbulence modeling for three-dimensional separation flows," *Physics of Fluids* **34**, 075101 (2022).
- <sup>7</sup>S. B. Pope, "A more general effective-viscosity hypothesis," *Journal of Fluid Mechanics* **72**, 331–340 (1975).
- <sup>8</sup>J.-L. Wu, H. Xiao, and E. Paterson, "Physics-informed machine learning approach for augmenting turbulence models: A comprehensive framework," *Phys. Rev. Fluids* **3**, 074602 (2018).
- <sup>9</sup>Y. Yin, P. Yang, Y. Zhang, H. Chen, and S. Fu, "Feature selection and processing of turbulence modeling based on an artificial neural network," *Physics of Fluids* **32**, 105117 (2020).
- <sup>10</sup>J. Ling, A. Kurzwaski, and J. Templeton, "Reynolds averaged turbulence modelling using deep neural networks with embedded invariance," *Journal of Fluid Mechanics* **807**, 155–166 (2016).
- <sup>11</sup>C. Jiang, R. Vinuesa, R. Chen, J. Mi, S. Laima, and H. Li, "An interpretable framework of data-driven turbulence modeling using deep neural networks," *Physics of Fluids* **33**, 055133 (2021).
- <sup>12</sup>W. Liu, J. Fang, S. Rolfo, C. Moulinec, and D. R. Emerson, "An iterative machine-learning framework for rans turbulence modeling," *International Journal of Heat and Fluid Flow* **90**, 108822 (2021).
- <sup>13</sup>Y. Cao, R. Xu, and P. Jiang, "Physics-informed machine learning based rans turbulence modeling convection heat transfer of supercritical pressure fluid," *International Journal of Heat and Mass Transfer* **201**, 123622 (2023).
- <sup>14</sup>H. Vaddireddy, A. Rasheed, A. E. Staples, and O. San, "Feature engineering and symbolic regression methods for detecting hidden physics from sparse sensor observation data," *Physics of Fluids* **32**, 015113 (2020).
- <sup>15</sup>F. Sofos, A. Charakopoulos, K. Papastamatiou, and T. E. Karakasidis, "A combined clustering/symbolic regression framework for fluid property prediction," *Physics of Fluids* **34**, 062004 (2022).
- <sup>16</sup>J. Weatheritt and R. Sandberg, "A novel evolutionary algorithm applied to algebraic modifications of the rans stress-strain relationship," *Journal of Computational Physics* **325**, 22–37 (2016).
- <sup>17</sup>Y. Zhao, H. D. Akolekar, J. Weatheritt, V. Michelassi, and R. D. Sandberg, "Rans turbulence model development using cfd-driven machine learning," *Journal of Computational Physics* **411**, 109413 (2020).
- <sup>18</sup>M. Schmelzer, R. P. Dwight, and P. Cinnella, "Discovery of algebraic reynolds-stress models using sparse symbolic regression," *Flow, Turbulence and Combustion* **104**, 579–603 (2020).
- <sup>19</sup>S. Beetham and J. Capecelatro, "Formulating turbulence closures using

- sparse regression with embedded form invariance,” *Phys. Rev. Fluids* **5**, 084611 (2020).
- <sup>20</sup>B. K. Petersen, M. L. Larma, T. N. Mundhenk, C. P. Santiago, S. K. Kim, and J. T. Kim, “Deep symbolic regression: Recovering mathematical expressions from data via risk-seeking policy gradients,” in *International Conference on Learning Representations* (2020).
- <sup>21</sup>G. Poesia, W. Dong, and N. Goodman, “Contrastive reinforcement learning of symbolic reasoning domains,” *Advances in Neural Information Processing Systems* **34**, 15946–15956 (2021).
- <sup>22</sup>R. S. Sutton and A. G. Barto, *Reinforcement learning: An introduction* (MIT Press, 2018).
- <sup>23</sup>L. Brunke, M. Greeff, A. W. Hall, Z. Yuan, S. Zhou, J. Panerati, and A. P. Schoellig, “Safe learning in robotics: From learning-based control to safe reinforcement learning,” *Annual Review of Control, Robotics, and Autonomous Systems* **5**, 411–444 (2022).
- <sup>24</sup>A. Fawzi, M. Balog, A. Huang, T. Hubert, B. Romera-Paredes, M. Barekatin, A. Novikov, F. J. R. Ruiz, J. Schrittwieser, G. Swirszcz, *et al.*, “Discovering faster matrix multiplication algorithms with reinforcement learning,” *Nature* **610**, 47–53 (2022).
- <sup>25</sup>D. Silver, J. Schrittwieser, K. Simonyan, I. Antonoglou, A. Huang, A. Guez, T. Hubert, L. Baker, M. Lai, A. Bolton, *et al.*, “Mastering the game of go without human knowledge,” *nature* **550**, 354–359 (2017).
- <sup>26</sup>J. Viquerat, P. Meliga, A. Larcher, and E. Hachem, “A review on deep reinforcement learning for fluid mechanics: An update,” *Physics of Fluids* **34**, 111301 (2022).
- <sup>27</sup>H. Yu, B. Liu, C. Wang, X. Liu, X.-Y. Lu, and H. Huang, “Deep-reinforcement-learning-based self-organization of freely undulatory swimmers,” *Phys. Rev. E* **105**, 045105 (2022).
- <sup>28</sup>S. Colabrese, K. Gustavsson, A. Celani, and L. Biferale, “Flow navigation by smart microswimmers via reinforcement learning,” *Physical Review Letters* **118**, 158004 (2017).
- <sup>29</sup>J. Rabault, M. Kuchta, A. Jensen, U. Réglade, and N. Cerardi, “Artificial neural networks trained through deep reinforcement learning discover control strategies for active flow control,” *Journal of Fluid Mechanics* **865**, 281–302 (2019).
- <sup>30</sup>J. Rabault and A. Kuhnle, “Accelerating deep reinforcement learning strategies of flow control through a multi-environment approach,” *Physics of Fluids* **31**, 094105 (2019).
- <sup>31</sup>H. Tang, J. Rabault, A. Kuhnle, Y. Wang, and T. Wang, “Robust active flow control over a range of reynolds numbers using an artificial neural network trained through deep reinforcement learning,” *Physics of Fluids* **32**, 053605 (2020).
- <sup>32</sup>Y.-Z. Wang, Y.-F. Mei, N. Aubry, Z. Chen, P. Wu, and W.-T. Wu, “Deep reinforcement learning based synthetic jet control on disturbed flow over airfoil,” *Physics of Fluids* **34**, 033606 (2022).
- <sup>33</sup>E. Hachem, H. Ghraieb, J. Viquerat, A. Larcher, and P. Meliga, “Deep reinforcement learning for the control of conjugate heat transfer,” *Journal of Computational Physics* **436**, 110317 (2021).
- <sup>34</sup>G. Beintema, A. Corbetta, L. Biferale, and F. Toschi, “Controlling rayleigh–bénard convection via reinforcement learning,” *Journal of Turbulence* **21**, 585–605 (2020).
- <sup>35</sup>R. Li, Y. Zhang, and H. Chen, “Learning the aerodynamic design of supercritical airfoils through deep reinforcement learning,” *AIAA Journal* **59**, 3988–4001 (2021).
- <sup>36</sup>J. Viquerat, J. Rabault, A. Kuhnle, H. Ghraieb, A. Larcher, and E. Hachem, “Direct shape optimization through deep reinforcement learning,” *Journal of Computational Physics* **428**, 110080 (2021).
- <sup>37</sup>G. Novati, H. L. de Laroussilhe, and P. Koumoutsakos, “Automating turbulence modelling by multi-agent reinforcement learning,” *Nature Machine Intelligence* **3**, 87–96 (2021).
- <sup>38</sup>J. Kim, H. Kim, J. Kim, and C. Lee, “Deep reinforcement learning for large-eddy simulation modeling in wall-bounded turbulence,” *Physics of Fluids* **34**, 105132 (2022).
- <sup>39</sup>H. J. Bae and P. Koumoutsakos, “Scientific multi-agent reinforcement learning for wall-models of turbulent flows,” *Nature Communications* **13**, 1–9 (2022).
- <sup>40</sup>M. Kurz, P. Offenhäuser, and A. Beck, “Deep reinforcement learning for turbulence modeling in large eddy simulations,” *International Journal of Heat and Fluid Flow* **99**, 109094 (2023).
- <sup>41</sup>B. E. Launder and B. I. Sharma, “Application of the energy-dissipation model of turbulence to the calculation of flow near a spinning disc,” *Letters in heat and mass transfer* **1**, 131–137 (1974).
- <sup>42</sup>C. Rudin, “Stop explaining black box machine learning models for high stakes decisions and use interpretable models instead,” *Nature Machine Intelligence* **1**, 206–215 (2019).
- <sup>43</sup>V. Belus, J. Rabault, J. Viquerat, Z. Che, E. Hachem, and U. Reglade, “Exploiting locality and translational invariance to design effective deep reinforcement learning control of the 1-dimensional unstable falling liquid film,” *AIP Advances* **9**, 125014 (2019).
- <sup>44</sup>J. N. Kutz, “Deep learning in fluid dynamics,” *Journal of Fluid Mechanics* **814**, 1–4 (2017).
- <sup>45</sup>N. Geneva and N. Zabararas, “Quantifying model form uncertainty in reynolds-averaged turbulence models with bayesian deep neural networks,” *Journal of Computational Physics* **383**, 125–147 (2019).
- <sup>46</sup>J. Wu, H. Xiao, R. Sun, and Q. Wang, “Reynolds-averaged navier–stokes equations with explicit data-driven reynolds stress closure can be ill-conditioned,” *Journal of Fluid Mechanics* **869**, 553–586 (2019).
- <sup>47</sup>B. P. Brener, M. A. Cruz, R. L. Thompson, and R. P. Anjos, “Conditioning and accurate solutions of reynolds average navier–stokes equations with data-driven turbulence closures,” *Journal of Fluid Mechanics* **915**, A110 (2021).
- <sup>48</sup>H. G. Weller, G. Tabor, H. Jasak, and C. Fureby, “A tensorial approach to computational continuum mechanics using object-oriented techniques,” *Computers in Physics* **12**, 620–631 (1998).
- <sup>49</sup>H. Xiao, J.-L. Wu, S. Laizet, and L. Duan, “Flows over periodic hills of parameterized geometries: A dataset for data-driven turbulence modeling from direct simulations,” *Computers & Fluids* **200**, 104431 (2020).
- <sup>50</sup>S. Jovic and D. M. Driver, “Backward-facing step measurements at low reynolds number,  $reh = 5000$ ,” *NASA technical memorandum* **108807**, 94035–1000 (1994).
- <sup>51</sup>H. Le, P. MOIN, and J. KIM, “Direct numerical simulation of turbulent flow over a backward-facing step,” *Journal of Fluid Mechanics* **330**, 349–374 (1997).
- <sup>52</sup>F.-A. Fortin, F.-M. D. Rainville, M.-A. Gardner, M. Parizeau, and C. Gagné, “Deap: Evolutionary algorithms made easy,” *Journal of Machine Learning Research* **13**, 2171–2175 (2012).
- <sup>53</sup>T.-H. Shih, *A realizable Reynolds stress algebraic equation model*, Vol. 105993 (National Aeronautics and Space Administration, 1993).
- <sup>54</sup>S. Banerjee, R. Krahl, F. Durst, and C. Zenger, “Presentation of anisotropy properties of turbulence, invariants versus eigenvalue approaches,” *Journal of Turbulence* **8**, N32 (2007).
- <sup>55</sup>R. L. Thompson, L. E. B. Sampaio, F. A. de Bragança Alves, L. Thais, and G. Mompean, “A methodology to evaluate statistical errors in dns data of plane channel flows,” *Computers & Fluids* **130**, 1–7 (2016).
- <sup>56</sup>X.-H. Zhou, J. Han, and H. Xiao, “Learning nonlocal constitutive models with neural networks,” *Computer Methods in Applied Mechanics and Engineering* **384**, 113927 (2021).
- <sup>57</sup>M. Abadi, A. Agarwal, P. Barham, E. Brevdo, Z. Chen, C. Citro, G. S. Corrado, A. Davis, J. Dean, M. Devin, S. Ghemawat, I. Goodfellow, A. Harp, G. Irving, M. Isard, R. Jozefowicz, Y. Jia, L. Kaiser, M. Kudlur, J. Levenberg, D. Mané, M. Schuster, R. Monga, S. Moore, D. Murray, C. Olah, J. Shlens, B. Steiner, I. Sutskever, K. Talwar, P. Tucker, V. Vanhoucke, V. Vasudevan, F. Viégas, O. Vinyals, P. Warden, M. Wattenberg, M. Wicke, Y. Yu, and X. Zheng, “TensorFlow, Large-scale machine learning on heterogeneous systems,” (2015).